

FRACTURE-MATRIX INTERFACE AREA CONTACTED BY
INJECTED FLUID AS A FUNCTION OF AVERAGE
SATURATION, MECHANICAL APERTURE AND COUNTER-
CURRENT IMBIBITION

A THESIS SUBMITTED TO THE DEPARTMENT OF MINERAL
RESOURCES AND PETROLEUM ENGINEERING IN PARTIAL
FULFILLMENT OF THE REQUIREMENTS FOR THE DEGREE OF
MASTER OF SCIENCE

Philipp Lang

2011

Affidavit

I declare in lieu of oath, that I wrote this thesis and performed the associated research myself, using only literature cited in this volume.

Eidesstattliche Erklärung

Ich erkläre an Eides statt, dass ich diese Arbeit selbstständig verfasst, andere als die angegebenen Quellen und Hilfsmittel nicht benutzt und mich auch sonst keiner unerlaubten Hilfsmittel bedient habe.

Date

Signature

Abstract

Capillary fluid transfer between fractures and water-wet siliclastic rock potentially is a vital contributor to achieving a high recovery from water flooding of Nelson's Type II Naturally Fractured Reservoirs (NFRs) where the rock matrix contains most of the hydrocarbon volume, but the fractures provide for the fluid pathways. This transfer, however, is restricted to the subset of fractures that is reached by the injected water.

Using a discrete fracture network model and a control volume finite element reservoir simulator, I compute the fracture surface area $A_{f,sw}(sw)$ where such a transfer occurs as a function of the pore volume of water injected into the fractured domain. We arrive at a nonlinear functional form for $A_{f,sw}(sw)$ by simulating a large number of meso-scale models with stochastically generated sets of well interconnected fractures. The simulation setup is constant rate water injection and constant pressure production. Fracture fluid transport is simulated with the Fourar-Lenormand two phase relative permeability models and affected by fracture-matrix fluid exchange modeled through nonlinear transfer functions. The fracture permeability is based on stress dependent fracture apertures.

Results show that the wetted portion of the fracture-matrix interface Area, $A_{f,sw}(sw)$, is affected not only by the viscosity contrast of injected and displaced fluid, but also by matrix capillary pressure responsible for the magnitude and time dependence of counter-current imbibition. The effects of this transfer on the shape

and velocity of propagation of the displacement front in the fracture network are shown. $A_{f,sw}(sw)$ serves as a new scaling parameter for fracture-matrix transfer in dual continuum models, potentially enhancing the predictive capabilities of this approach.

Kurzfassung

Kapillardruck bedingter Phasenaustausch zwischen Klüften und der umgebenden wasser-benetzenden siliklastischen Matrix stellt einen bedeutenden Recovery Mechanismus dar, besonders für als Nelsons Typ II eingestufte Lagerstätten, in denen der Großteil des Fließens in den Klüften statt findet und die Matrix als Kohlenwasserstoffspeicher dient. Dieser Austausch ist jedoch begrenzt durch den Teil der Klüfte, der vom Waterflood erreicht wird. Einer Abschätzung dieses Anteils gilt diese Arbeit.

Basierend auf Discrete Fracture Network Simulationsmodellen und einem Finite Volumen-Finite Elemente Simulator wird die erreichte Kluft-Matrix Fläche untersucht und in Abhängigkeit von injiziertem Porenvolumen und Matriceigenschaften dargestellt.

Die resultierende Fläche $A_{f,sw}(sw)$ wird als Funktion abgeleitet aus Ergebnissen zahlreicher Simulationen von meso-großen Lagerstättenmodellen mit stochastisch generierten Kluftsets mit ausgeprägter Konnektivität. Alle Simulationen wurden als Viertel-Ausschnitt eines invertierten Five-Spot Musters ausgelegt, mit konstanter Injektionsrate und Fördersondendruck. Zur Berechnung der relativen Permeabilitäten der Phasen in den Klüften wurde das Fourar-Lenormand Model verwendet. Um den Transfer von Öl und Wasser zwischen Kluft und Matrix zu simulieren, ist eine nicht-lineare Transferfunktion eingebaut worden. Die Fracture

Permeabilitäten sind direkt proportional ihrer Weite, die aus einem vom Spannungszustand bestimmten Model errechnet werden.

Die sich ergebende Formulierung für den benetzten Anteil der Gesamtkluftfläche, $A_{f,sw}(sw)$, ist nicht alleine abhängig vom Viskositätsverhältnis der verpumpten und produzierten Phase sowie der Injektionsrate, sondern vor allem durch die Kapillardruckverhältnisse in Matrix und Klüften, die bestimmend sind für das Ausmaß and Fluss zwischen Fractures und umgebenden Porenraum. Zusätzlich wird die Verlangsamung der Displacement Front und die Veränderung ihrer Form und Penetrationsstärke in Abhängigkeit der Counter-Current Imbibition dargestellt.

Der erhaltene Parameter $A_{f,sw}(sw)$ stellt einen möglichen Parameter für Dual-Continuum Simulationen dar, welcher helfen kann der Sensitivität gegenüber Injektionsraten Rechnung zu tragen, und die Vorhersagequalität solcher Modelle heben sollte.

Acknowledgements

I would like to express my sincere gratitude to my supervisor, Prof. S.K. Matthäi. May this be the beginning to a prolific collaboration for years to come.

Contents

- List of Figures ix
- List of Tables xiii
- List of Acronyms xiv
- 1 Introduction 1
- 2 Methodology 4
 - 2.1 Simulation Models 5
 - 2.1.1 Discrete Fracture Networks 6
 - 2.1.2 Simulation Setup 8
 - 2.1.3 Mechanically Controlled Fracture Aperture 10
 - 2.1.4 Model FRACS133 13
 - 2.1.5 Model FRACS60 14
 - 2.1.6 Model JOLLY 15
 - 2.2 CSMP++ DFN Simulator 16
 - 2.2.1 Governing Equations 18
 - 2.2.2 Finite Element – Finite Volume Discretization 20
 - 2.2.3 Property Scaling For Lower Dimensional Fracture Representations 21
 - 2.2.4 Fracture Flow 22
 - 2.2.5 Fracture Matrix Transfer 26
 - 2.2.6 Transient Simulation 31
 - 2.2.7 Evaluation 35
- 3 Results 36
 - 3.1 Results in 1D - Effects of Fracture-Matrix Transfer on Advection 36
 - 3.2 Results in 2D – Flow in a Single Fracture 40
 - 3.2.1 Low Injection Rate, High Matrix Permeability 41
 - 3.2.2 Low Injection Rate, Low Matrix Permeability 43
 - 3.2.3 High Injection Rate, High Matrix Permeability 44
 - 3.2.4 High Injection Rate, Low Matrix Permeability 45
 - 3.3 Results in 3D – Discrete Fracture Network Simulations 46
 - 3.3.1 Flow Channeling through NFRs due to Spatial Conductivity Variations 47
 - 3.3.2 JOLLY 47

3.3.3	FRACS60.....	51
4	Discussion	54
5	List of References.....	55
6	Appendix.....	57

List of Figures

Figure 1: Discrete Fracture Network finite element model in ICEM CFD(Ansys). Rock fractures are modeled explicitly (discs), as they provide the flow domain. The matrix is considered to provide storage capacity only, and is accounted for through a mathematical representation..... 6

Figure 2: Triangular finite element mesh of a fracture cluster. Lower dimensional representation means an area modeling what actually constitutes a volume, i.e. an area with given thickness. The width(or aperture, thickness) of a fracture is accounted for by the means of variables, discretized at the element. 7

Figure 3: FracMan (Goldman Inc.) Graphical User Interface. The bounding box, which represents the simulation model domain, is populated stochastically with two sets of fractures. 8

Figure 4: Inverted Five-Spot Pattern; simulation setups used in this thesis represent a quarter (shadowed), featuring an injector-producer pair. The extend of the diagonal of the models is between 125 and 500 m..... 9

Figure 5: Principle stresses and initial fluid pressure applied to the simulation models. The z-axis in the cartesian coordinate system points represents depth. The full stress tensor is outlined with its components on the right. 10

Figure 6: Using the far field stress regime imposed onto the model, normal and shear stress is computed for each fracture element by means of projection..... 11

Figure 7: The position of each finite element within the fracture is determined to account for its thinning out towards the tips. Hence, the maximum fracture aperture will be in its center. The positional aperture distribution then is scaled by the ration of fluid pressure versus normal stress, also accounting for failure in shear. 12

Figure 8: Cruikshank apertures for full(left) and by layering truncated(right) fracture. The scale, indicating permeability, is direct proportional to the computed fracture aperture through the parallel plate law..... 13

Figure 9: FRACS133 DFN model. Two sets with constant dip and azimuth intersect at a 35 degree angle. The spacing between injector and producer is about 70 m. It contains 54791 triangular surface elements with 27490 nodes. 14

Figure 10: FRACS60 DFN model, featuring two sets with Fisher distributed dip and azimuth. Fracture size is power law distributed. It features 41865 triangular surface elements with 20201 nodes. 15

Figure 11: JOLLY DFN model. Fracture size is power law distributed. Two fracture sets populate the reservoir domain, which extends over 200x200x50m. Element count is 38082 with a total of 16710 nodes. 16

Figure 12: Fracture length distribution observed in NFRs after Lauterbach et al. 1997. Power law generation algorithms in FracMan populate the domain with fracture sizes along the straight line. 16

Figure 13: General outline of the initialization phase. Initializing the model imposing boundary conditions; assigning material properties), solving for an initial pressure state; establishing of a stress state acting on the domain and computation of the resulting mechanically controlled fracture apertures, calculating the initial velocity and proceeding with the transient simulation routine. 18

Figure 14: Finite element - finite volume mesh. This hybrid discretization is peculiar to CSMP++. 20


Figure 15: Fourar-Lenormand viscous coupling relative permeability model (1998), using a viscosity ration between non-wetting and wetting fluid of 1.5. The red and blue lines indicate non-wetting and wetting relative permeability respectively. The black line represents the sum  manifests itself by greater than unity sum of relperms. 24

Figure 16: Mobilities derived from the Fourar-Lenormand (1998) viscous coupling model. Blue and red indicate wetting and non-wetting phase mobility, the black line represents the total mobility. 25

Figure 17: Fractional flow curve (blue) and its derivative with respect to saturation (black) plotted versus saturation. Note that due to the viscous coupling phenomenon, the fractional flow of the wetting phase exceeds unity. 26

Figure 18: Relation of fracture aperture (twice r) to matrix capillary entry pressure and depth of invasion. 27

Figure 19: Oil saturation in the matrix interface versus depth of invasion over time. The gradient (black line) at $x \sim 0$ is the driving force to counter-current imbibition. It decreases in magnitude with the duration of transfer, owing to a saturation drop due to imbibition. 28

Figure 20: Fracture Matrix Transfer function – the dependence of the transfer magnitude on the interface saturation and duration of transfer is illustrated. The apex is located around intermediate interface saturation, and declines exponentially with time. 29

Figure 21: Evaluating transfer magnitude for spectra of matrix permeability and saturation. The largest phase exchange between fracture and matrix is actually found at higher matrix permeabilities. 29

Figure 22: The FMT Algorithm within our CSMP++ DFN Simulator. To calculate the magnitude of the exchange term, transfer duration has to be established to find the saturation in the virtual matrix adjacent to each fracture element. 31

Figure 23: Transient Simulation loop. Implicit solution of saturation (the non-wetting phase is advected). Update of the wetting phase saturation and recalculation of saturation

<i>dependent flow properties such as mobility. Implicit solution of pressure, calculation of velocity as post processing step.</i>	<i>32</i>
<i>Figure 24: Introducing source/sink terms due to fracture-matrix transfer brings a degree of non-linearity to the transport equation. In colored background the elements of the Picard loop are highlighted. After calculating the transfer term, saturation is reset to its state after the previous iteration. The convergence criterion is fulfilled once the saturation of the previous iteration and the current saturation distribution do not deviate above a certain threshold. ...</i>	<i>34</i>
<i>Figure 25: One dimensional waterflood from left to right (Buckley-Leverett profile). On the abscissa: distance in m. On the ordinate: Saturation with respect to water. Initially, the entire domain is fully oil saturated. An imposed pressure difference between the left and right boundary, along with a constant water saturation of 1.0 at the left causes displacement. Blue squares indicate transport without any source terms acting, red dots represent flow accounting for fracture matrix transfer by means of a source term acting on the flooded portion of the domain. The output interval with respect to time remains constant.</i>	<i>37</i>
<i>Figure 26: 1D simulations for various front speeds. From top to bottom: 1.0E-8, 1.0-9 and 1.0E-11 ms⁻¹ respectively. The difference between transport without any sink term (blue curve) and accounting for sink terms gets larger increasingly.....</i>	<i>39</i>
<i>Figure 27: Top: Front advancement with (red) and without (blue) counter-current imbibition. Bottom: The magnitude of the sink term with respect to water for the corresponding front position. Note the exponential decline of the sink term away from the newly swept region (towards the left).</i>	<i>40</i>
<i>Figure 28: 2D Low rate, high matrix permeability scenario. On the left: 2D visualization of oil saturation. On the right: Oil saturation in 1D along the x-axis of the corresponding 2D plot on the left – After 7 hours of displacement from right to left. The flood front in the fracture with fracture-matrix transfer(bottom) already lags behind by about 50%.</i>	<i>42</i>
<i>Figure 29: Illustration of transfer magnitude between the water in the fractures and the oil residing in the virtual matrix. In the transport algorithm implemented in CSMP++ by Matthäi, Geiger et al., this source term is referred to as nodal fluid volume source, as it is discretized at the nodes. Bottom right shows a 1D plot of nodal fluid volume source along the fracture's x-axis. The front is at its halfway point.....</i>	<i>43</i>
<i>Figure 30: Comparison plot of the saturation distribution in fractures with different matrix permeabilities. Top: High conductivity matrix after 7 hours of water flooding from left to right. Bottom: Low conductivity matrix at the same time. The front is further advanced due to less phase exchange.....</i>	<i>44</i>
<i>Figure 31: Advection in a single fracture for high injection rates. Top: no fracture-matrix transfer. Bottom: Transfer with a virtual matrix of relatively high conductivity.</i>	<i>45</i>
<i>Figure 32: Oil drained into the fracture from the adjacent matrix until breakthrough for all 2D scenarios described in this section. Generally speaking, low injection rates attract more oil</i>	

from the pore space. Low IR, High $k(m)$ in blue; Low IR, Low $k(m)$ in red. High IR, High $k(m)$ in purple, High IR, Low $k(m)$ in green..... 46

Figure 33: Flow focusing in a trivialized fracture network. Velocity distribution is far from being uniform. Flow is higher around high conductivity fractures (either due to size and/or orientation relative to stress field) and near the center of fractures..... 47

Figure 34: JOLLY after 4.1 hours of waterflooding from the bottom left to the upper right of the cube shaped domain. Left: fluid pressure distribution. Middle: saturation distribution at time of breakthrough. Right: Wetted area of the fracture network (21%). 48

Figure 35: Saturation distribution for JOLLY at breakthrough (after 12.5 hrs) for high injection rate with high matrix permeability. On the right: wetted fraction of total contact area (14%). Note also the higher oil saturation behind the front..... 48

Figure 36: High injection rate (182 m³/day) and low matrix permeability (1 mD): Less transfer leads to less retardation in breakthrough (8.3 hours), a lower oil saturation behind the front and more fracture area contacted by the injected fluid (26%). 49

Figure 37: Plot of wetted fracture surface area vs. fracture volume injected..... 50

Figure 38: Average water saturation behind the front for FRACS60. Only fractures wetted by the injected fluid are considered in this average..... 51

Figure 39: Drained oil volume for FRACS60 vs. time until breakthrough..... 52

Figure 40: FRACS60 model at time of breakthrough. Left side shows saturation (top) and transfer (bottom) for the highly conductive matrix. On the right hand side: low conductivity results. Transfer in both cases is the highest in newly swept regions..... 53

Figure 41: Comparison of fraction of surface area wetted at time of breakthrough for different setups in JOLLY..... 57

List of Tables

Table 1: Properties common to all simulation runs. 10

Table 2: Common settings for all 2D fracture simulations..... 41

Table 3: Breakthrough times for different 2D simulation scenarios. The difference between high and low permeability matrix front speed is greater for low injection rates (slow front advancement). 45

Table 4: Simualtion results JOLLY with FMT and various parameters..... 50

List of Acronyms

DFN	Discrete Fracture Network
CSMP++	Complex System Modeling Platform
FMT	Fracture Matrix Transfer
REV	Representative Elementary Volume
C++	Object Oriented Programming Language
IMPIMS	Implicit Pressure Implicit Saturation
FE	Finite Element
FV	Finite Volume
PVI	Pore Volume Injected

1 Introduction

Conventional thinking on numerical simulation of naturally fractured reservoirs (NFR) is subdued by multi-continua approaches. Fractures and matrix are treated as distinct entities, even though residing in identical grid blocks, with their interaction being captured by so called transfer functions. Flow due to viscous pressure gradients may either occur in both, matrix and fractures (dual permeability), or only within the fractured domain (dual porosity). Based on a statistical network description, usually restricted to density and permeability of fractures, an effective permeability is averaged across grid blocks and a storage capacity for hydrocarbons is assigned (Warren and Root, 1963; Kazemi et al., 1976). This averaging of permeability over cells with an extent of up to a couple of hundred meters in diameter implicitly assumes the applicability of a representative elementary volume (REV).


Recent literature, however, strongly indicates that such a REV with respect to flow behavior does not exist (Matthäi et al, 2009; Paluszny et al., 2007). Rather, the non-uniform nature of fractures with respect to conductivity, geometry/orientation and density along with the tendency to occur in sets demands for different means of accommodation. This thesis will deal with a less obvious obstacle to the dual-porosity approach as it is implemented in most proprietary reservoir simulation applications. In Nelson Type II fractured reservoirs, the porous rock matrix acts as hydrocarbon storage whereas the fracture network provide for phase transport due

to a viscous gradient (Nelson, 1982). Recovery in such a reservoir is controlled by the ability to drain oil to the fracture flow system from its adjacent matrix by means of capillary forces (fracture-matrix transfer, FMT). This exchange of phases is caused by the preference of the matrix to the water phase as opposed to the oil phase, being initially saturated with the latter. In case of water wet rock, the injected wetting fluid will imbibe the matrix through the fracture surface area. This exchange between phases is conventionally accommodated for by means of the earlier mentioned transfer function. Naturally, this transfer only occurs at that fraction of the surface which actually is in contact with the injected fluid. This contacted area, however, is assumed to be constant by the dual-porosity approach. In this thesis I will show, by means of numerical simulation, that the amount of fracture-matrix interface area which allows for transfer is dependent on flow velocity and matrix properties. Results also reflect the influence of fracture conductivity that is not uniform, but rather a function of fracture geometry and orientation in relation to the far-field stress state which is present in reservoirs of all kind. Fracture network geometry is retained and accounted for by means of discrete fracture modeling.

I will start out by introducing to the CSMP++ based control volume finite element simulator (Matthäi et al., 2009; Geiger et al., 2003; Paluszny et al., 2007). It was developed to capture behavior of discrete fracture networks (DFN), accounting for fracture-matrix exchange by means of a transfer function similar to the approach presented, but with some simplifications. DFN models chosen for evaluation runs are, as will be shown, well connected networks with power-law distributed fracture

size. The models are of meso-scale size, i.e. up to 300 meters in diameter. Setups reflect a quarter of a five-spot pattern, featuring an injector-producer pair with constant rate and pressure conditions, respectively. The workflow applied to arrive at the results presented is laid out and the formulations for fracture flow and transfer are presented. In the results section, I will illustrate the effects of fluid transfer on flow in general and within single fractures and well-connected fracture networks. By considering fracture network geometry, the more realistic distribution of influencing variables and different setups, an attempt is made to capture the nature of the fraction of interface area contacted by the injected fluid.

2 Methodology

The problem at hand was approached by means of numerical simulation. Using the CSMP++ library, I developed a control volume finite element (Geiger et al., 2003) based simulator within the C++ programming language. Flow Phenomena accounted for in this simulator include viscous displacement, capillary spreading within the fractures and transfer of phases between fracture and adjacent matrix. I restricted the number of phases to two, a water-oil system as found in undersaturated reservoirs. The numerical solution technique of choice was IMPIMS, referring to the sequential implicit solution of both pressure and saturation. A proprietary algebraic multigrid solver (SAMG, Fraunhofer) is used to solve the systems of equation (Stüben, 1999; Stüben et al., 2003). Simulation models base on discrete fracture network (DFN) geometries from Goldman's FracMan (Flynn and Pine, 2007) and a finite element discretization (ICEM CFD, Ansys) accounting for fluid pressure and relative stress state. While flow through the network is simulated using the above approach, an exchange of phases between the  by means of a non-linear transfer function that acts as source/sink in the transport equation (Unsal et al., 2009). This is done in an effort to account for counter-current imbibition during e.g. waterflooding of an oil saturated water-wet fractured reservoir. The area of fracture elements in contact with the displacing phase is calculated and output versus the amount of injected volume.

2.1 Simulation Models

Any reservoir simulation workflow starts out with an adequate geometrical representation of the domain of interest. Using computer aided tools, a more or less detailed model is generated based on a thorough characterization of the geology at hand. In the case of natural fractures, this is far from being trivial due to a number of reasons:

- The fracture surface to thickness aspect ratio is extremely large (fracture aperture in the range of micrometers, reservoir extend in the range of kilometers)
- Fractures might displace adjacent layers due to lateral movement (shear displacement)
- Focus of flow inside the fractures due to their likely high permeability

The discrete modeling of fractures is an approach investigated in great detail and count by recent literature (Hugo et al., 2004; Rogers et al., 2010). Especially in Nelson reservoirs of Type II and higher, interconnected fractures constitute the dominant flow paths, and capturing the flow phenomena within them provides major insight into the dynamic nature of such a reservoir. The approach of choice is to model flow inside the fractures only, and considering the matrix to be a mere accommodator of hydrocarbons. This might be considered an equivalent to the dual porosity approach, but as shown in the

results section, it might be considered superior in both, its predictive and illustrative capabilities when simulating fractured reservoir behavior.

The geological model of the fracture network is consequently discretized in space using a finite element mesh. Material properties, such as fracture conductivity, are assigned and initial conditions applied, imposing a given simulation setup on the model.

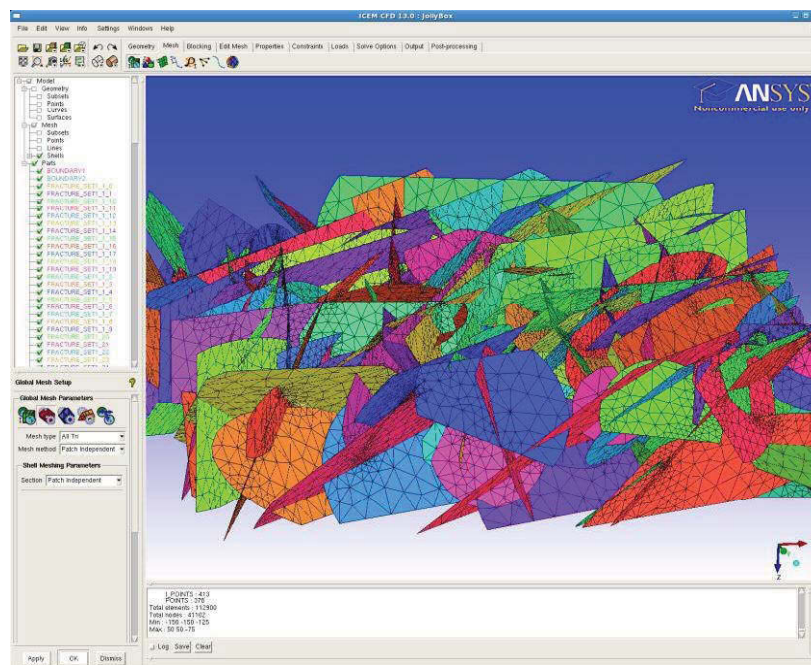


Figure 1: Discrete Fracture Network finite element model in ICEM CFD(Ansys). Rock fractures are modeled explicitly (discs), as they provide the flow domain. The matrix is considered to provide storage capacity only, and is accounted for through a mathematical representation.

2.1.1 Discrete Fracture Networks

The fracture representation of choice in this thesis is an explicit one of lower dimensional finite elements (Unsal et al., 2009; Matthäi et al. 2007). In essence, we model a fracture with extend in three dimensions using planar elements (surfaces) located in 3D space, such that the shape and orientation of the fracture is modeled

explicitly, and the thickness is accounted for by means of variables attributed to each fracture element. The models presented in this thesis are comprised exclusively of triangular finite elements.

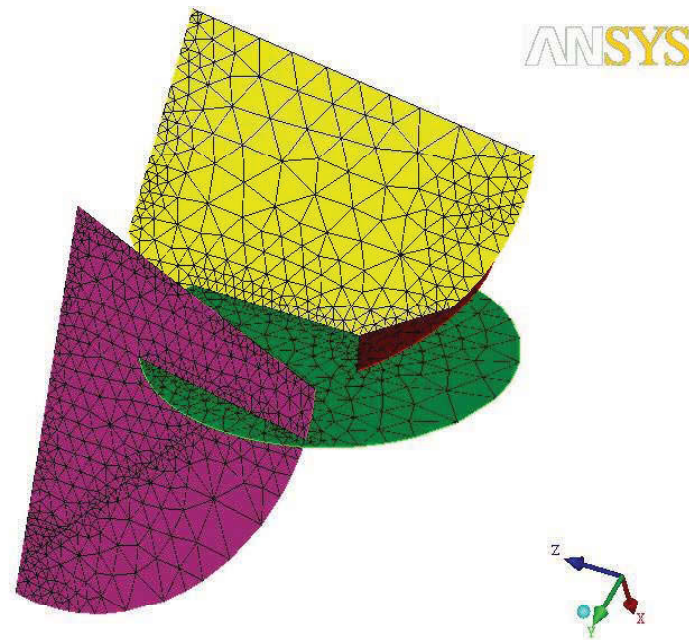


Figure 2: Triangular finite element mesh of a fracture cluster. Lower dimensional representation means an area modeling what actually constitutes a volume, i.e. an area with given thickness. The width (or aperture, thickness) of a fracture is accounted for by the means of variables, discretized at the element.

The advantages of a discrete fracture network representation start with the ability to retain the major flow paths in a geometrically proper manner. Orientation and size of fractures are accounted for. Compared to discrete fracture discrete matrix models, mesh element count is reduced by one to two orders of magnitude (Unsal et al., 2009) and the meshing procedure itself spares a lot of complexity. On the downside, alternative means have to be found to accommodate matrix behavior which influences the dynamic of a full scale reservoir. Conventional dual continua models feature an explicit volume representing the matrix and its behavior, and

functions which couple the interactions between fracture and matrix. In this thesis I use a mathematical function to accommodate the behavior of what is referred to as virtual matrix.

Fracture Geometries were created using FracMan by Goldman Inc. in a stochastic manner. The bounding domain is of box shape for all models. The fracture network is comprised of multiple fracture sets, which are groups of fractures with individual distributions for size, orientation and count. Most models used in this thesis feature about two to four sets of fractures. After stochastically populating the domain, sets are screened for fractures that are not interconnected. These orphan fractures are removed from the model.

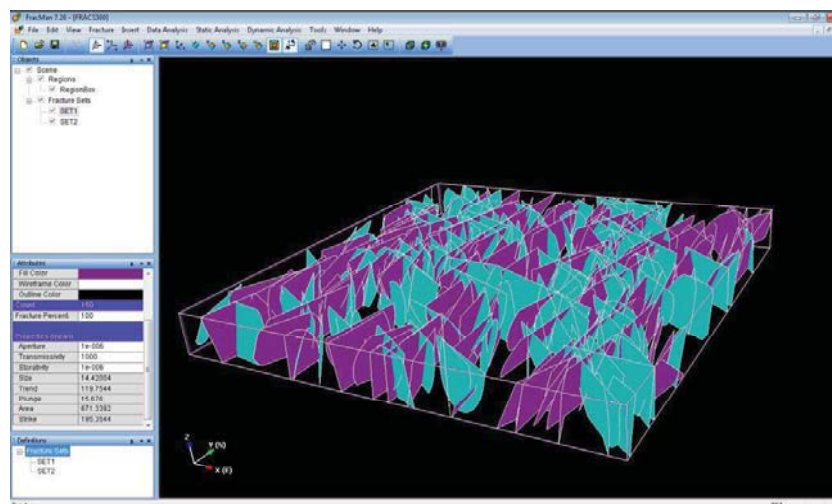


Figure 3: FracMan (Goldman Inc.) Graphical User Interface. The bounding box, which represents the simulation model domain, is populated stochastically with two sets of fractures.

2.1.2 Simulation Setup

A quarter of an inverted five-spot pattern (Figure 4) was used in all of my simulation runs. An injector-producer pair at opposing edges in the cube shaped

meso-scale reservoir models provided for through-flow. Constant rate boundary conditions represented the water injecting well, whereas the producers were set to constant pressure.

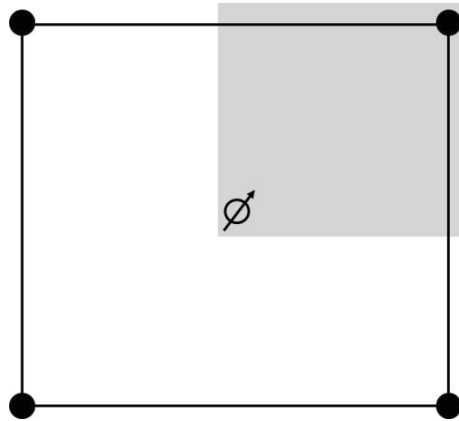


Figure 4: Inverted Five-Spot Pattern; simulation setups used in this thesis represent a quarter (shaded), featuring an injector-producer pair. The extent of the diagonal of the models is between 125 and 500 m.

Fracture flow properties, such as aperture, porosity and permeability, result from a given underground stress state (see section on mechanically controlled fracture apertures). An Andersonian Normal Faulting stress state was imposed on all models, supposing a reservoir in 3000 m of depth and an average overburden rock density of 2400 kg/m³. Initial fluid pressure is assumed to be hydrostatic, with a fluid density of 1000 kg/m³. The resulting far field stress tensor and pressure is illustrated in Figure 5. For convenience, I aligned the principle stresses with the Cartesian coordinate system.

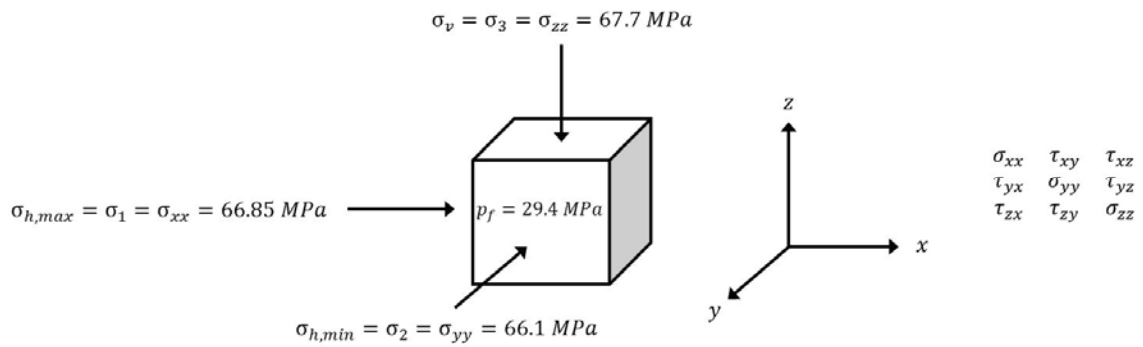


Figure 5: Principle stresses and initial fluid pressure applied to the simulation models. The z-axis in the Cartesian coordinate system points represents depth. The full stress tensor is outlined with its components on the right.

Fluid properties, such as density and viscosity, remained unchanged for all runs. Fractures are considered to have no residual saturations of either phase. Initially, all models are fully oil saturated. Table 1 summarizes the common initial conditions and constant properties as they apply to all runs over the entire duration of simulation. Rock properties also remain constant for all models.

total system compressibility	[Pa ⁻¹]	1.0E-9
oil density	[kg/m ³]	800.0
water density	[kg/m ³]	1000.0
oil viscosity	[Pa.sec]	0.005
water viscosity	[Pa.sec]	0.001
residual saturation oil	[-]	0.0
residual saturation water	[-]	0.0
initial oil saturation	[-]	1.0

Table 1: Properties common to all simulation runs.

2.1.3 Mechanically Controlled Fracture Aperture

Discrete Fractures used in simulation models in this thesis are of disc or truncated disc shape. They are represented by surface elements, which account for the aperture of the fracture by the use of a variable, namely fracture aperture,

discretized at the element. Element variables are piecewise constant, that means fracture aperture is considered as constant over for the entire element, but may vary over the extend of the fracture, since a fracture is discretized to a number of finite elements (Figure 2). Each individual fracture gets assigned a unique aperture distribution on its elements, depending on size, initial internal fluid pressure and orientation/location with respect to the far field stress state.

Once the initial fluid pressure has been established, a subroutine within the initialization phase of the simulator computes the acting normal stress vector for each surface element from the global stress tensor along with the shear stress components (Figure 6). This is done by plain tensor transformation with respect to the surface orientation of each fracture element.

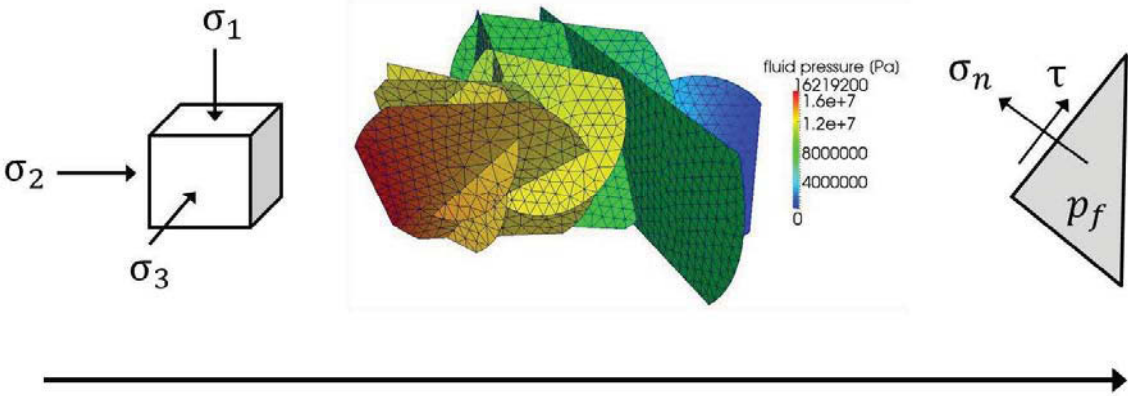


Figure 6: Using the far field stress regime imposed onto the model, normal and shear stress is computed for each fracture element by means of projection.

Now that normal and shear stress components have been established, the distance of e ~~parenting fracture~~ parenting fracture and the shortest distance to the boundary are computed (Figure 7). This is done in an effort to

prepare for the next step, in which each element gets assigned an aperture depending on its position within the fracture, and the ratio between normal and shear stress

Figure 7).

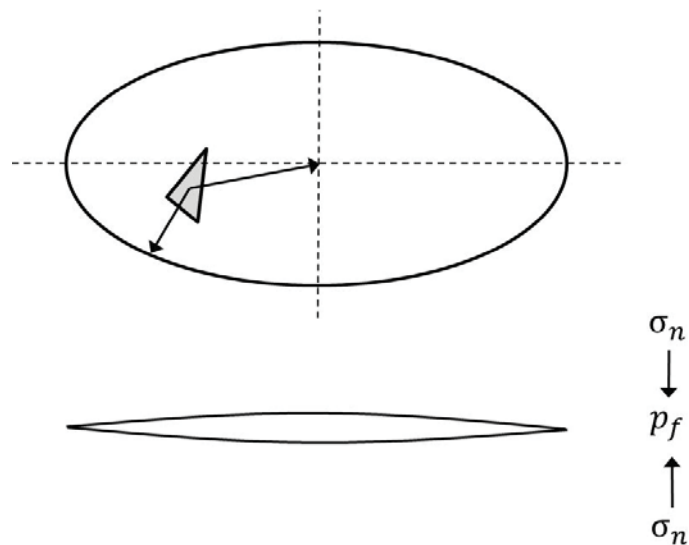


Figure 7: The position of each finite element within the fracture is determined to account for its thinning out towards the tips. Hence, the maximum fracture aperture will be in its center. The positional aperture distribution then is scaled by the ratio of fluid pressure versus normal stress, also accounting for failure in shear.

This mechanical fracture aperture algorithm was implemented in CSMP++ by Stephan K. Matthäi in 2006 and follows an outline of Cruikshank et al. in 1991. The routine starts out by establishing a fracture radius, an equivalent to the extent of the fracture, which is later used to scale the maximum aperture. As a next step the shear to normal stress ratio for each element is computed and the fracture evaluated against shear failure (Jaeger and Cook, 1979, using a friction coefficient μ_c of 0.05):

$$\tau = \mu_c * (\sigma_n - p_f) \quad \text{Equation 1}$$

If τ is greater than the far field shear stress acting on the fracture element, the fracture is assumed to fail due to shear. The opening of the fracture either way is arrived at by evaluating the two equations (Cruikshank et al. 1991):

$$W = 2 * (-\sigma_n + p_f) * \frac{1 - \nu}{\mu} * \sqrt{\text{radius}^2 - \text{distance_to_center}^2} \quad \text{Equation 2}$$

$$U = 2 * \tau * \frac{1 - \nu}{\mu} * \sqrt{\text{fracture_radius}^2 - \text{distance_to_center}^2} \quad \text{Equation 3}$$

Equation 2 calculates the opening of the fracture with respect to the normal stress to fluid pressure balance and position within the fracture. Equation 3 calculates the shear displacement of the fracture which, to arrive at a resulting dilatation, is multiplied by a factor of 0.4 (Moab rule, Cruikshank et al. 1991). Whichever value is greater, W or $U*0.4$, gets assigned as fracture aperture to the element. Figure 8 illustrates the resulting aperture distribution for a full and a truncated single fracture.

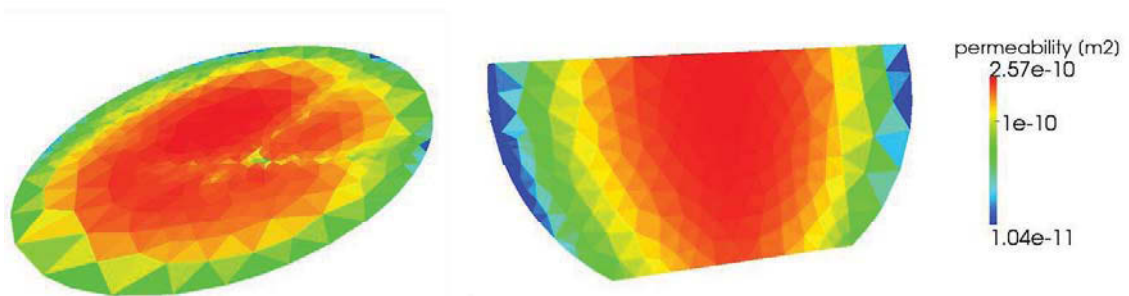


Figure 8: Cruikshank apertures for full (left) and by layering truncated (right) fracture. The scale, indicating permeability, is direct proportional to the computed fracture aperture through the parallel plate law.

2.1.4 Model FRACS133

This DFN model contains two distinct set of fractures, intersecting each other at a 35 degree angle. Fracture size is uniformly distributed between 7 and 13 m in diameter, azimuth (0 and 35 degrees) and dip (0 degrees) are constant. Fracture height is truncated due to a vertical extension of the bounding box of 10 m. Fracture surface area for set 1 and 2 equals 167.12 and 164.2 square meter, respectively. Total fracture count is 133 (71 for set 1 and 62 for set 2). Areal dimension is 50x50 m.

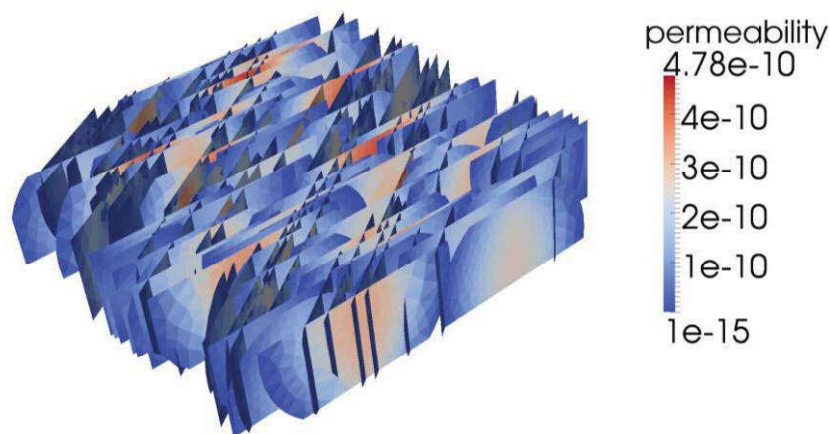


Figure 9: FRACS133 DFN model. Two sets with constant dip and azimuth intersect at a 35 degree angle. The spacing between injector and producer is about 70 m. It contains 54791 triangular surface elements with 27490 nodes.

2.1.5 Model FRACS60

FRACS60 obeys to a power law distribution in fracture size (Laubach et al. 1997). Two fracture sets with 30 fractures each between 5 and 15 m in diameter populate a domain of 50x50x15 m. Fractures cover a total area of 528.8 square meters, with 30 fractures in both sets. The mean azimuth is 85 and 35 degrees for set 1 and set 2, respectively. Mean dip for both sets is 15 degrees. Azimuth and dip is Fisher distributed with a dispersion of 15.

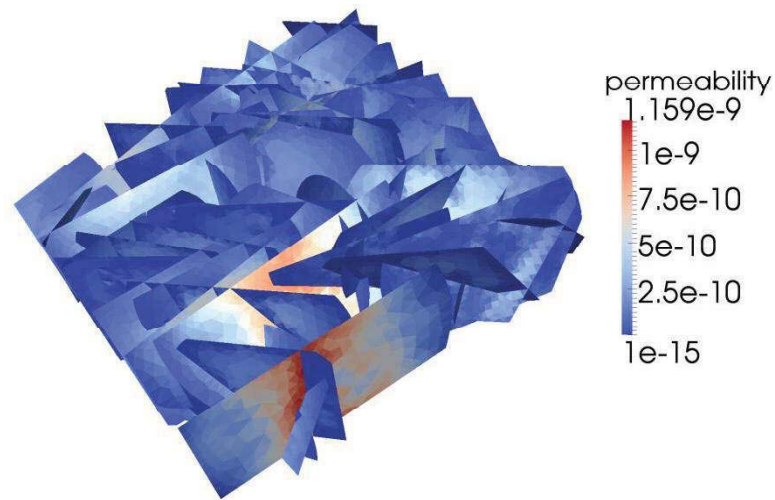


Figure 10: FRACS60 DFN model, featuring two sets with Fisher distributed dip and azimuth. Fracture size is power law distributed. It features 41865 triangular surface elements with 20201 nodes.

2.1.6 Model JOLLY

The JOLLY DFN model was adapted from Jolly et al. 2000. It comprises two fracture sets with a mean dip of 0 degrees and mean azimuth of 135 and 45 degrees for set 1 and 2, respectively. These means are applied to a Fisher distribution with a dispersion factor of 15. Fractures size is power law distributed (Laubach et al. 1997) between 10 and 20 m. Fracture intensity is described by a P32 value (square meter of fracture surface per cubic meter of domain volume) of 0.08. Model dimensions are 200x200x50m.

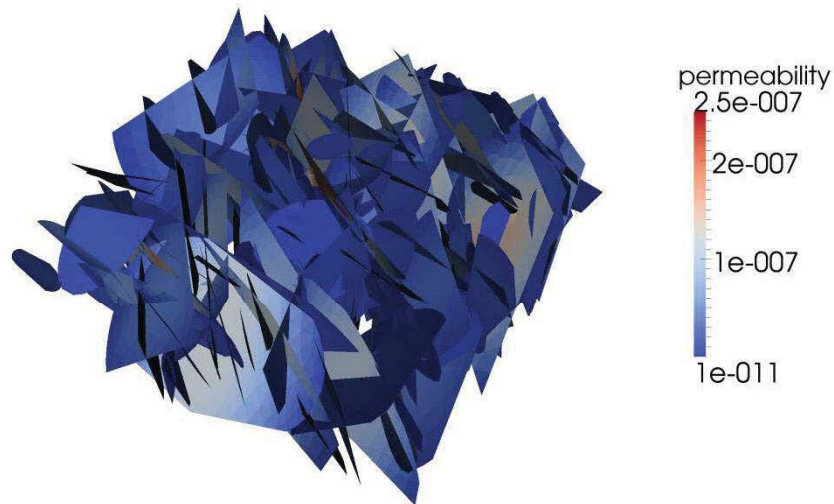


Figure 11: JOLLY DFN model. Fracture size is power law distributed. Two fracture sets populate the reservoir domain, which extends over 200x200x50m. Element count is 38082 with a total of 16710 nodes.

The higher values in permeability for this model compared to FRACS133 and FRACS60 is due to the larger fracture size. The power law distribution in fracture length (Figure 12) is set to diameters between 5 and 85 m. This model is the largest one used in this thesis, with an injector producer spacing of about 280 m.

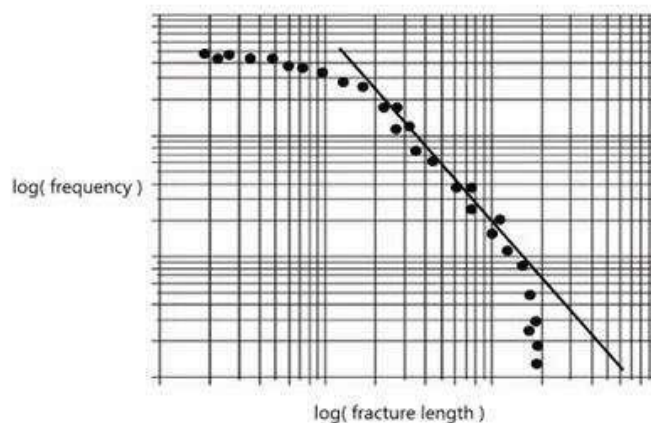


Figure 12: Fracture length distribution observed in NFRs after Lauterbach et al. 1997. Power law generation algorithms in FracMan populate the domain with fracture sizes along the straight line.

2.2 CSMP++ DFN Simulator

Following the reading in of the finite element mesh is a configuration phase in which the initial and boundary conditions of choice are imposed onto the simulation model. The total mobility according to the phase saturation distribution is calculated which then allows the simulator to solve for preliminary pressure. A stress regime acting on the far field scale is established and fracture permeability is calculated based on a mechanical aperture model accounting for fluid pressure and relative stress state. The resulting absolute permeabilities finally allow for the computation of a velocity field, which together with the initial pressure and saturation distribution is provided as a starting point to the transient computation.

Transient computation mode refers to the iterative algorithm within the simulator which is repeated until a final simulation outcome is achieved. My implementation first solves for saturation and pressure sequentially and iteratively, which is followed by an update of saturation dependent flow properties such as relative permeability, total mobility and velocity. In case of fracture-matrix transfer, a non-linear Picard loop is integrated which iterates the computation of the saturation dependent exchange term and the computation of saturation dependent flow properties and saturation transport.

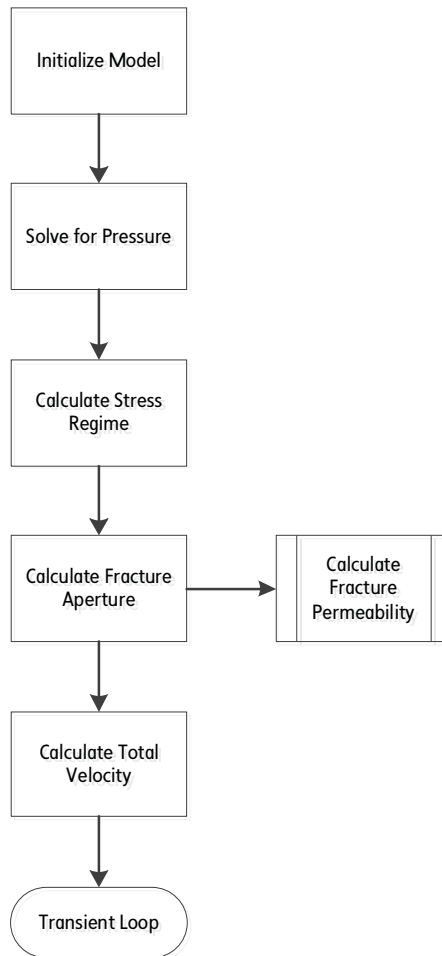


Figure 13: General outline of the initialization phase. Initializing the model imposing boundary conditions; assigning material properties), solving for an initial pressure state; establishing of a stress state acting on the domain and computation of the resulting mechanically controlled fracture apertures, calculating the initial velocity and proceeding with the transient simulation routine.

2.2.1 Governing Equations

Flow within the fracture network is considered incompressible and steady-state in nature. Combining the first-principle law of mass conservation and the Darcy constitutive relationship, we obtain the elliptic partial differential equation (PDE)

$$\nabla(k_f \lambda_t \nabla p) + q = 0 \tag{Equation 4}$$

This equation for pressure diffusion factors in the saturation dependent total mobility of the phases as well as the intrinsic fracture permeability, which I will come

back to in greater detail when the mechanically controlled aperture calculation is discussed. The term q in Equation 4 is an imposed flux at a model boundary in case of Rate-Pressure setups, as discussed in the DFN simulation model section. It is zero at any other point in the domain.

Saturation transport over time is realized by solving for advection of a single phase and consequently updating of the other, which in a two-phase black oil simulation with water and oil being the sole actors is trivial since

$$\sum_{\alpha=1}^2 S_{\alpha} = 1 \quad \text{Equation 5}$$

is obvious. The hyperbolic PDE governing the global matrix for transport of one phase is given by a Buckley-Leverett solution to the transient multiphase flow problem, arising from the conservation of mass, the concept of saturation in a porous medium containing more than one phase and, of course, Darcy's law, which gives

$$\phi \frac{\partial S_{\alpha}}{\partial t} + v_t \frac{df_{\alpha}}{dS_{\alpha}} \nabla S_{\alpha} + q_{fmt} = 0 \quad \text{Equation 6}$$

with q_{fmt} as the imposed flux between the fracture and the matrix:

$$q_{fmt} \rightarrow q_{fmt}(x, y, z, t, s) \quad \text{Equation 7}$$

In Addition to the fractional flow term, this introduces a high degree of non-linearity to our saturation function. I will elaborate in more detail the nature of this transfer term and its iterative solution approach when the concept of fracture-matrix transfer is discussed.

2.2.2 Finite Element – Finite Volume Discretization

While solving for pressure and saturation sequentially and fully implicitly, the simulator makes use of a dual discretization scheme implemented in CSMP++ and introduced to by many authors in recent literature (Geiger et al., 2004; Paluszny et al. 2007). In essence, the finite element mesh generated by ANSYS Icem CFD is superimposed with a node-centered finite volume mesh during the initialization phase of the transport algorithm (Figure 14).

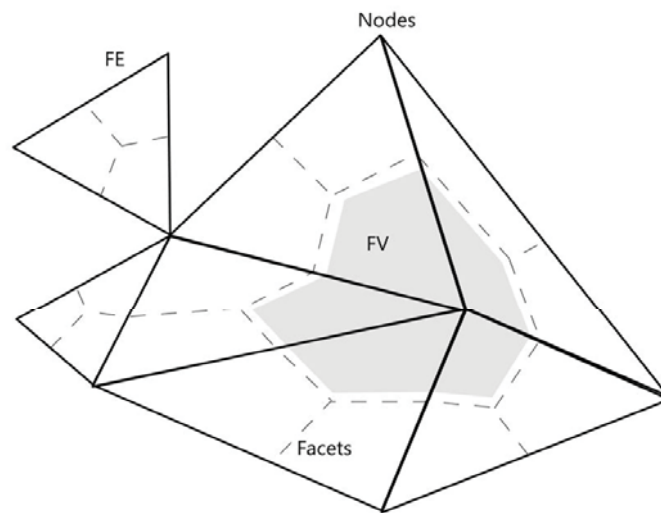


Figure 14: Finite element - finite volume mesh. This hybrid discretization is peculiar to CSMP++.

Finite volumes are created around finite element nodes. In the process, finite elements are split into what is referred to as sectors in CSMP++ terminology. Each FE features as many sectors as nodes and each FV is comprised of as many sectors as its center node has parent elements. The elliptic pressure equation (Equation 4) is solved for in terms of a finite element approach, whereas the hyperbolic mass balance equation (Equation 6) is dealt with using the finite volume method (Chung, 2002).

Pressure and saturation at the FE and FV, respectively, are approximated by piecewise linear and piecewise constant integration functions (Nick et al., 2010).

2.2.3 Property Scaling For Lower Dimensional Fracture Representations

Since, as pointed out earlier, fractures are represented as surfaces using planar elements in 3D space, means of scaling have to be applied to produce realistic flow behavior (Paluszny et al., 2007). Both element properties, porosity and permeability, are multiplied by the fracture aperture to compensate for the missing volumetric extend of the elements. Since the porosity of a fracture is unity, obeying

applied. Apertures are found in the range of 0.001 m or 1 mm, which makes porosity accordingly small. This in turn renders the transient part of (Equation 6) very small and increases the advective part accordingly. This hyperbolic part of the saturation equation underlies, even though solved implicitly, in some way the Courant-Friedrichs-Lewy condition.

$$\frac{u \Delta t}{\Delta x} < C \quad \text{Equation 8}$$

The finite element mesh in Figure 2 shows that in order to retain the network geometry and model intersections properly, local refinement of element size has to be used. Both, the small element size and the large advective contribution in the transport equation, result in small timesteps that had to be chosen to produce correct results. Vast overstepping of this time increment, even though a fully implicit numerical solution approach was used, results in incorrect front speeds when

accounting for fracture-matrix transfer by means of a source term in (Equation 6). We found that in order not to interfere with proper convergence, time increments about 25% below the lowest Courant number found in the model had to be chosen. Simulations that did not account for counter-current imbibition between fracture and matrix, meaning that no source/sink terms were applied, did not underlie this restriction.

2.2.4 Fracture Flow

The intrinsic (absolute, single phase) permeability of a fracture with constant hydraulic aperture a and smooth walls is given by Witherspoon et al. (1980):

$$k_f = \frac{a^2}{12} \quad \text{Equation 9}$$

We assume laminar creeping two-phase flow inside the fractures, deeming inertial forces negligible.

applies using the concept of relative permeabilities, which yields

$$v_t = \mathbf{k} \lambda_t \nabla p \quad \text{Equation 10}$$

as an expression for the total Darcy velocity inside the fracture (neglecting gravity and buoyancy forces); based on the concept of phase mobility, where, assuming constant viscosity, we find that

$$\lambda_\alpha = \frac{k_{r,\alpha}}{\mu_\alpha} \rightarrow \lambda_\alpha(S_\alpha) \quad \text{Equation 11}$$

which in the case of immiscible two-phase flow may lead to a total mobility

$$\lambda_t = \sum_{\alpha=1}^2 \lambda_{\alpha} \quad \text{Equation 12}$$

Fourar and Lenormand (1998) evaluated flow experiments emulating such conditions and proposed a relative permeability model accounting for viscous coupling between two immiscible fluids in fracture flow. For the wetting phase relative permeability they found that

$$k_{r,w} = \frac{S_w^2}{2} (3 - S_w) \quad \text{Equation 13}$$

and for the non-wetting phase

$$k_{r,w} = \frac{S_w^2}{2} (3 - S_w) \quad \text{Equation 14}$$

$$k_{r,nw} = (1 - S_w)^3 + \frac{3\mu_{nw}}{2\mu_w} S_w (1 - S_w) (2 - S_w) \quad \text{Equation 15}$$

This formulation opposes the linear saturation to relative permeability relationship for two-phase flow in fractures, proposed by Romm (1966) and consequent authors. We use the Fourar-Lenormand approach, in which each fluid acts on the ability of the other to flow by exerting a drag like effect due to viscous coupling. This mechanism also is well known in near wellbore gas condensate wells (Henderson et al., 1997 and 2000). Hence, the sum of the relative permeabilities may exceed unity, depending on the viscosity ration, as illustrated in Figure 15.

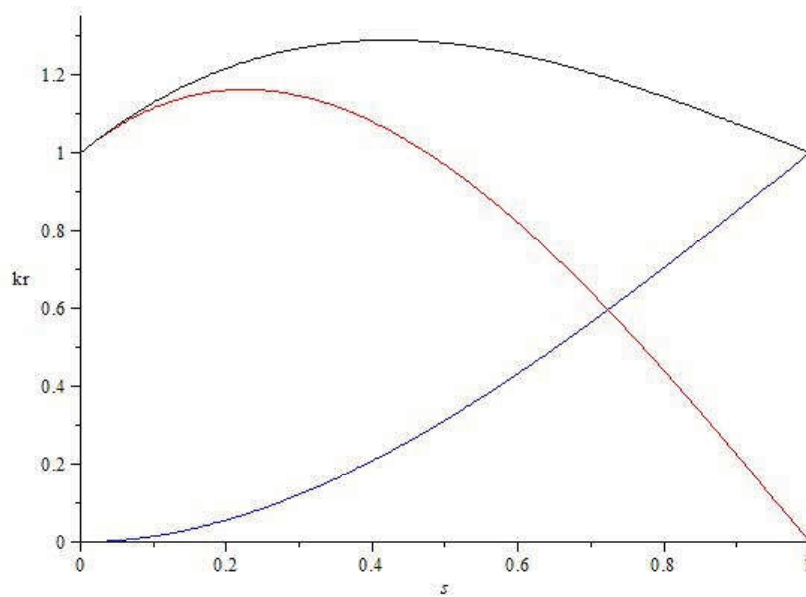


Figure 15: Fourar-Lenormand viscous coupling relative permeability model (1998), using a viscosity ratio between non-wetting and wetting fluid of 1.5. The red and blue lines indicate non-wetting and wetting relative permeability respectively. viscous drag which manifests itself by greater than unity sum of relperms.

Mobilities resulting from Figure 15, using a viscosity ratio of 1.5, are presented in Figure 16.

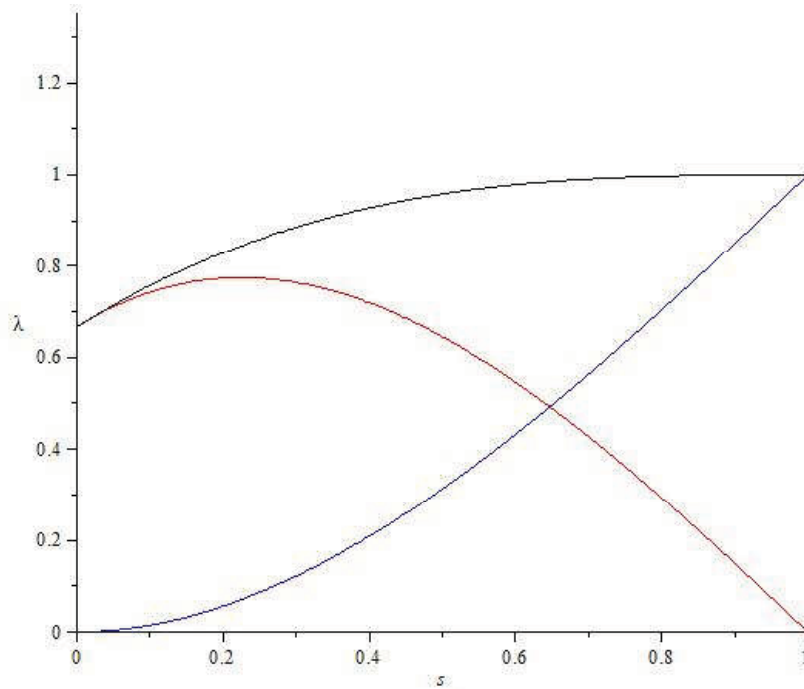


Figure 16: Mobilities derived from the Fourar-Lenormand (1998) viscous coupling model. Blue and red indicate wetting and non-wetting phase mobility; the black line represents the total mobility.

The total mobility is authoritative to the calculation of the total filtration velocity as in equation (Equation 10) as well as to the fractional flow and its derivative w.r.t. saturation used in the transport equation (Equation 6), where the former is given by

$$f_w = \frac{\lambda_w}{\lambda_t} \quad \text{Equation 16}$$

which is illustrated in Figure 17 alongside its derivative

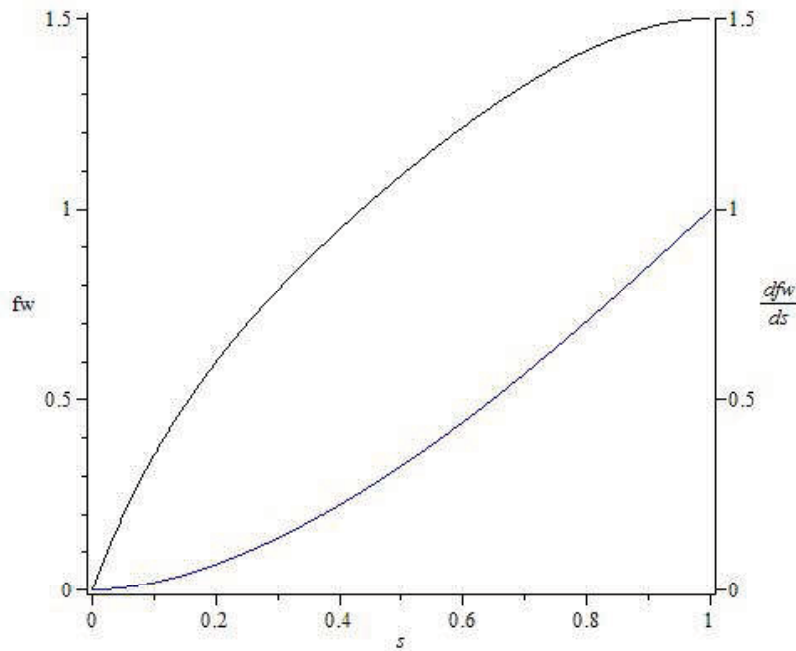


Figure 17: Fractional flow curve (blue) and its derivative with respect to saturation (black) plotted versus saturation. Note that due to the viscous coupling phenomenon, the fractional flow of the wetting phase exceeds unity.

2.2.5 Fracture Matrix Transfer

A water wet rock, saturated with non-wetting phase, will imbibe once exposed to wetting phase saturation. This phenomenon is generally referred to as spontaneous imbibition. Waterflooding of such a reservoir, in this thesis categorized ~~as~~ will cause an exchange of wetting phase (displacing phase) with non-wetting phase (displaced phase) between the fracture and its adjacent matrix. We quantified the magnitude of this exchange per unit area of fracture-matrix interface as

$$q_{fmt} = \bar{\lambda}(S_w^{IF}) k_m \frac{p_c^m(S_w^{IF}) - p_c^f(a)}{\Delta x} \quad \text{Equation 17}$$

This is the source/sink term acting on our transport equation (Equation 6). Its driving gradient is that of difference in capillary pressure between the fracture $p_c^f(a)$

and the matrix $p_c^m(S_w^{IF})$, normalized by the depth of invasion of the wetting phase into the matrix block, Δx or half the aperture of the fracture (Figure 18).

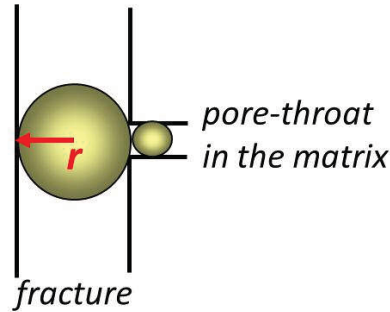


Figure 18: Relation of fracture aperture (twice r) to matrix capillary entry pressure and depth of invasion.

Brooks-Corey capillary pressure curves are used to find p_c^m for a given saturation in dependence on the matrix permeability and porosity, using a Leverett-J like factor $\frac{k}{\phi}$ (representing pore size distribution) to relate p_c^m accordingly. The capillary pressure inside the fracture is given by the Young-Laplace equation for capillary tubes, so that, for a given fracture aperture a ,

$$p_c^f(a) = \frac{\sigma \ 4 \cos \theta}{a} \quad \text{Equation 18}$$

is constant, i.e. independent of the saturation.

S_w^{IF} is the wetting phase saturation at the interface is assumed to obey a diffusion type behavior over time (Figure 19).

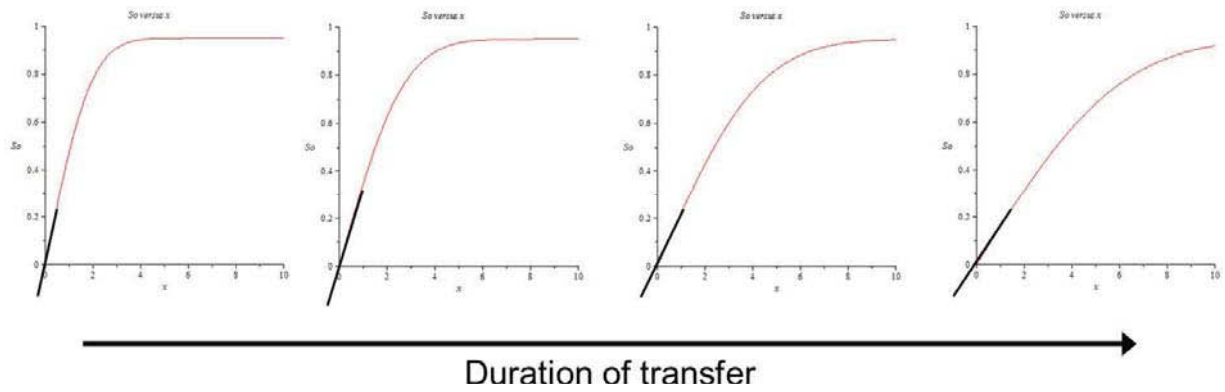


Figure 19: Oil saturation in the matrix interface versus depth of invasion over time. The gradient (black line) at $x = 0$ is the driving force to counter-current imbibition. It decreases in magnitude with the duration of transfer, owing to a saturation drop due to imbibition.

This behavior is approximated by an error function based expression in 1D (perpendicular to the fracture interface)

$$S_w(x, t) = S_{wi} \operatorname{erfc} \frac{x}{2\sqrt{kt}} \quad \text{Equation 19}$$

The relation between $q_{fmt} \rightarrow q_{fmt}(S_w^{IF})$ and $S_w^{IF} \rightarrow S_w^{IF}(x, t)$ is illustrated in Figure 20. An exponential like decline of the source term magnitude with increasing duration of transfer is characteristic to our implementation of fracture-matrix exchange.

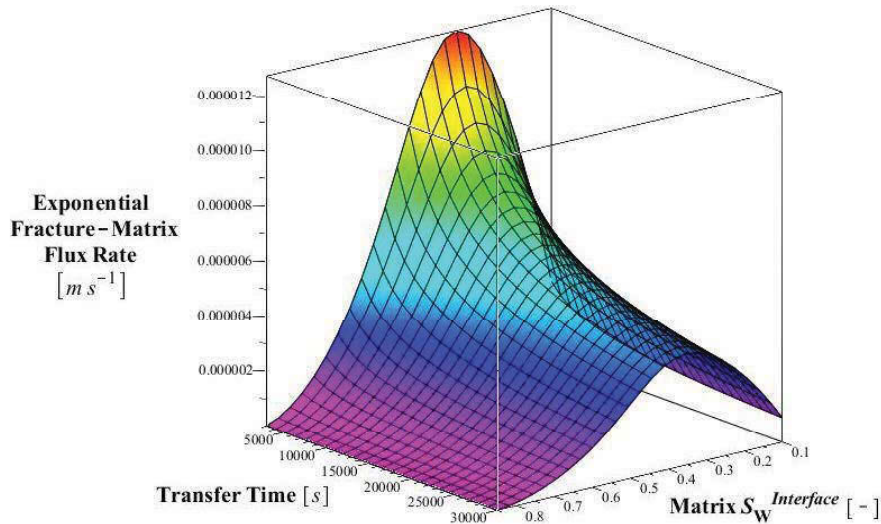


Figure 20: Fracture Matrix Transfer function – the dependence of the transfer magnitude on the interface saturation and duration of transfer is illustrated. The apex is located around intermediate interface saturation, and declines exponentially with time.

Evaluating Equation 17 for different matrix permeabilities reveals that transfer is the largest at larger matrix permeabilities (Figure 21). In order to evaluate the impact of counter-current imbibition, simulation runs were performed using a spectrum of matrix permeabilities and porosities.

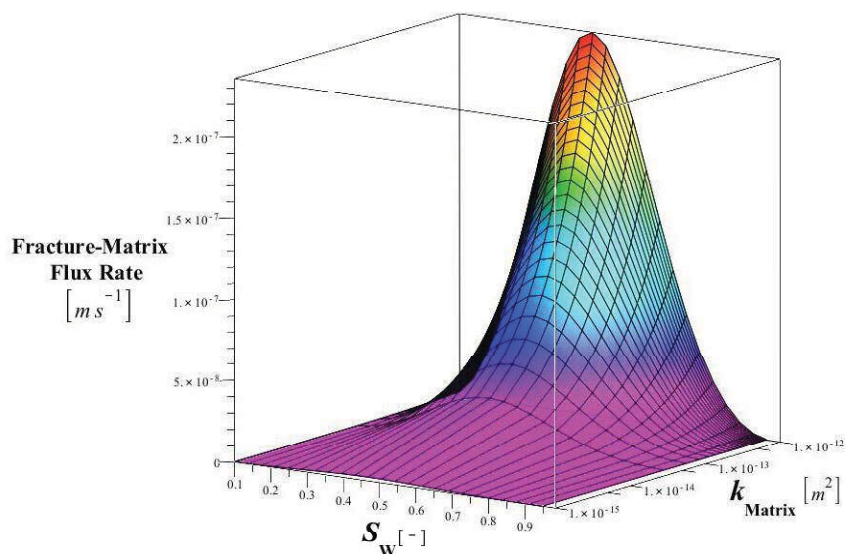


Figure 21: Evaluating transfer magnitude for spectra of matrix permeability and saturation. The largest phase exchange between fracture and matrix is actually found at higher matrix permeabilities.

My fracture matrix transfer algorithm (Figure 22) loops over all fracture elements to check whether the displacement front already reached this part of the model. It does so by comparing the current saturation against a certain saturation threshold, which I usually set to the residual wetting phase saturation (in case of a fracture, this would be zero) plus an arbitrary value of 15 %. If the fracture element has been reached by the displacing fluid for the first time, the algorithm stores the current simulation time as initial time for fracture matrix transfer. For subsequent iterations (see chapter on the Transient Simulation part), this time value is subtracted from the current simulation time to calculate the duration of transport, which goes into Equation 19 to establish the saturation in the virtual matrix block and hence determines the magnitude of the current transfer rate (Equation 17).

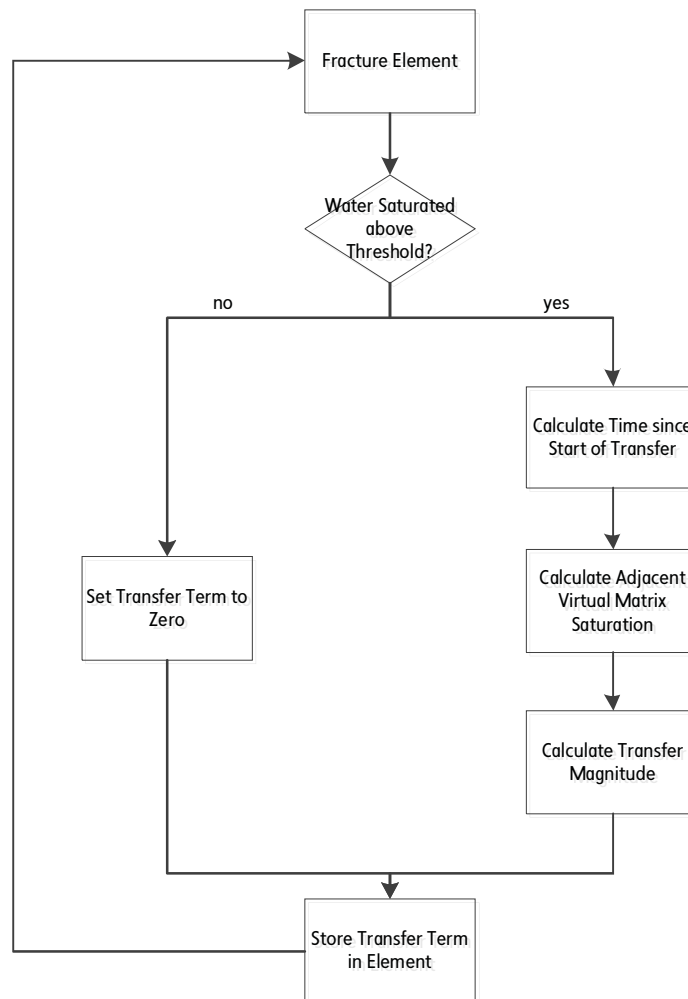


Figure 22: The FMT Algorithm within our CSMP++ DFN Simulator. To calculate the magnitude of the exchange term, transfer duration has to be established to find the saturation in the virtual matrix adjacent to each fracture element.

The algorithm also accounts for the case of seizing transfer: this is when due to a lack of wetting fluid influx compared to influx of non-wetting fluid from the virtual matrix, the saturation drops below the threshold. Fracture-matrix therefore halts, i.e. is set to zero for upcoming iterations.

2.2.6 Transient Simulation

The transient computation part of my simulator refers to the algorithm that advances the saturation over the domain in time. In order to establish a reference

case to assess the impact of counter-current imbibition on the qualitative and quantitative nature of the displacement front, two realizations are implemented. The default algorithm accounts for fracture-matrix transfer, whereas an alternative

The latter may represent fluid flow through fractured granite basement, whereas the former is what we argue to be flow within fractures (Nelson, 1982). Figure 23 is a schematic of the general layout of my simulation algorithm, not accounting for the non-linear transfer term in Equation 6.

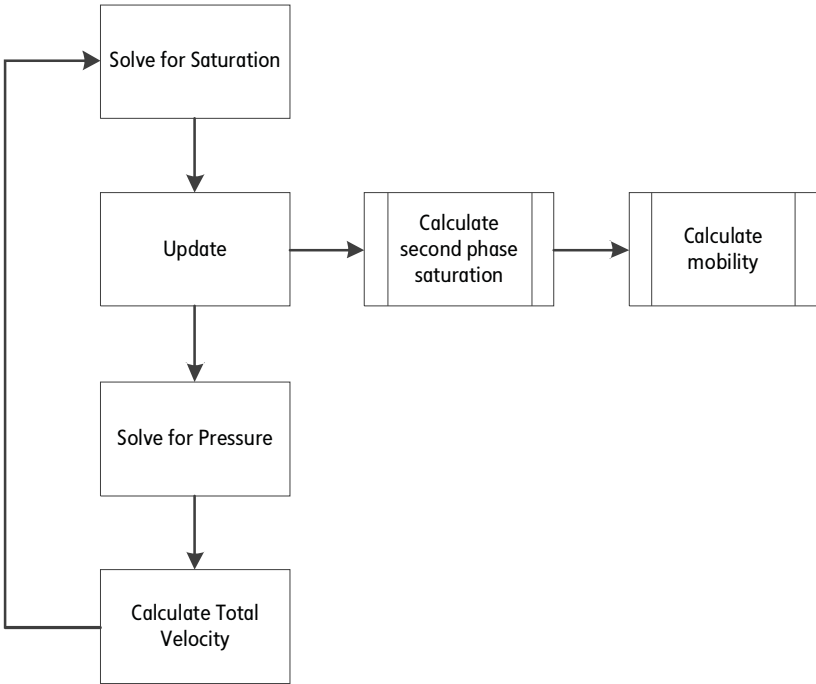


Figure 23: Transient Simulation loop. Implicit solution of saturation (the non-wetting phase is advected). Update of the wetting phase saturation and recalculation of saturation dependent flow properties such as mobility. Implicit solution of pressure, calculation of velocity as post processing step.

Any pre- and post-processing during simulation is applied before the start or after the end of this loop, respectively. Output and analysis happen after each cycle. The current model time is advanced by the time increment during post processing,

which in turn gets updated based on the change in saturation due to velocity changes during the last time step (CFL approach). The implicit solution strategy allows solving multiple scalar problems sequentially as opposed to single, larger coupled systems at once (Stüben et al., 2003). This reduces the degree of non-linearity substantially. Introducing a source/sink term to the advection equation, as is the case for fracture flow obeying to fracture-matrix transfer, will cause a mutual dependency of saturation (its transport) and the source/sink term (its magnitude). We tackled this non-linear behavior by introducing a Picard loop. Figure 24 illustrates the extended version of the transient simulation loop:

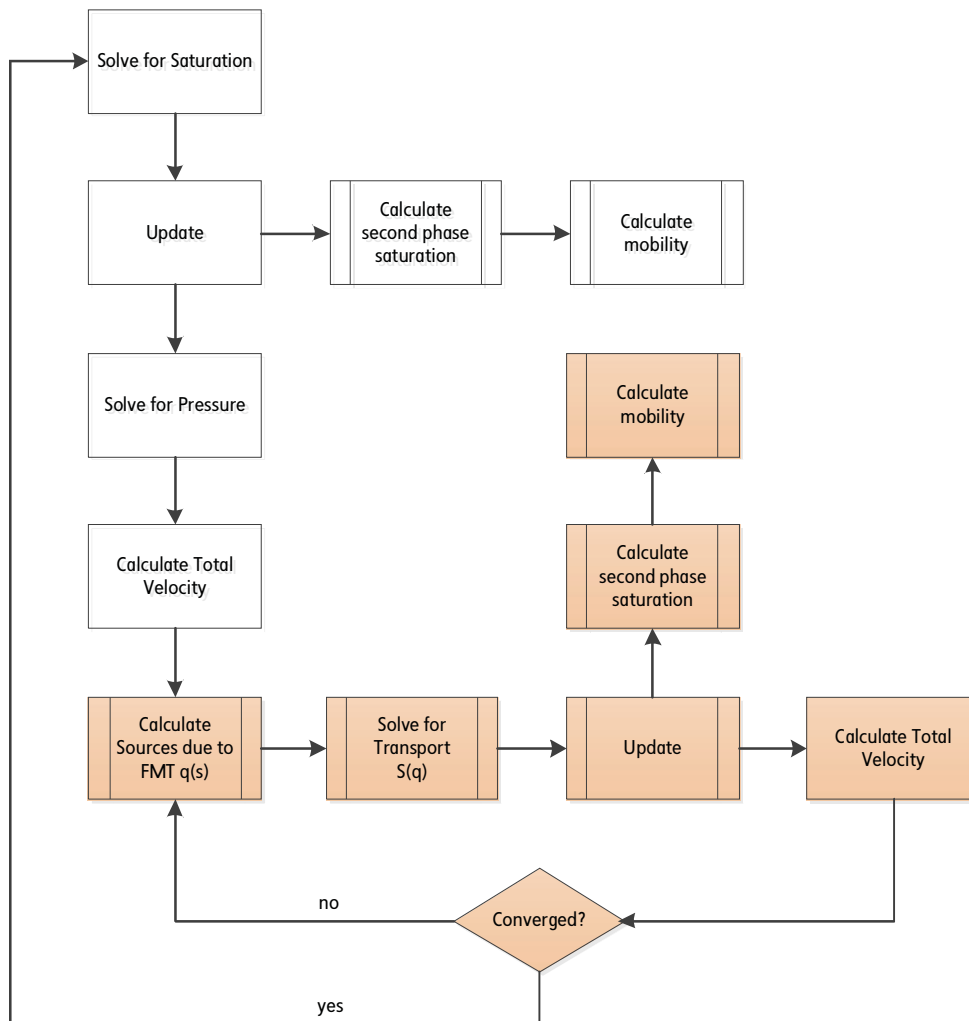


Figure 24: Introducing source/sink terms due to fracture-matrix transfer brings a degree of non-linearity to the transport equation. In colored background the elements of the Picard loop are highlighted. After calculating the transfer term, saturation is reset to its state after the previous iteration. The convergence criterion is fulfilled once the saturation of the previous iteration and the current saturation distribution do not deviate above a certain threshold.

To calculate the convergence of a Picard iteration, the scalar field of non-wetting phase saturation is stored before entering the non-linear loop initially, and the after

resulting saturation field of the last iteration. I established two criteria here: a maximum difference, which finds the element with the highest discrepancy, and an average difference, which calculates the arithmetically averaged difference of all elements in contact with the displacing fluid. If the convergence criterion (usually

around 1-5% in saturation) has not been fulfilled, the saturation field is reset to its initial state and the next iteration is initiated.

2.2.7 Evaluation

The calculation of fracture-matrix interface area contacted by the displacing fluid is a straight forward one. A dedicated algorithm within the course of post processing loops over all fracture elements and declares them as wetted once the saturation at any time increases above a threshold (see Fracture Matrix Transfer). Even if saturation drops below this threshold due to a halt of the front and ongoing transfer, the element remains accounted for as contacted in consequent analysis runs. After each transient simulation step, contacted interface area is recorded together with simulation time and boundary influx, i.e. injected volume. This volume is normalized by the domain pore volume, resulting in pore volume injected (PVI).

3 Results

Verification of our conceptual model and numerical scheme was performed by comparing results in 1D and 2D against solutions in MatLab, Maple, CMG and a new Transport Scheme developed in CSMP++ by Shaho Bazrafkan in 2011. Also results in one and two dimensions allow observing the influence of fracture-matrix transfer on saturation transport. Most notably is the change in saturation over time as well as a change in front velocity.

Once we were confident in our ability to simulate behavior such as front advancement and saturation change behind the front due to counter-current imbibition in dependence of various parameters, meso-scale model simulation runs were performed.

3.1 Results in 1D - Effects of Fracture-Matrix Transfer on Advection

In order to verify that the simulator is able to capture the effects of source/sink terms on multiphase transport properly, I started out with creating a one dimensional Buckley-Leverett simulator prototype using the proprietary mathematics tool suite Maple. A domain of 10 m in length was set out to be fully oil saturated (residual saturations equal zero). A pressure difference was applied to impose a left to right waterflood. Since the generic design of the CSMP++ suite allows switching seamlessly between one, two or three dimensional applications, I started

out with runs in one dimension. Figure 25 shows saturation over distance for a 1D model with an extension of 10 meters discretized to 101 nodes or 100 line elements.

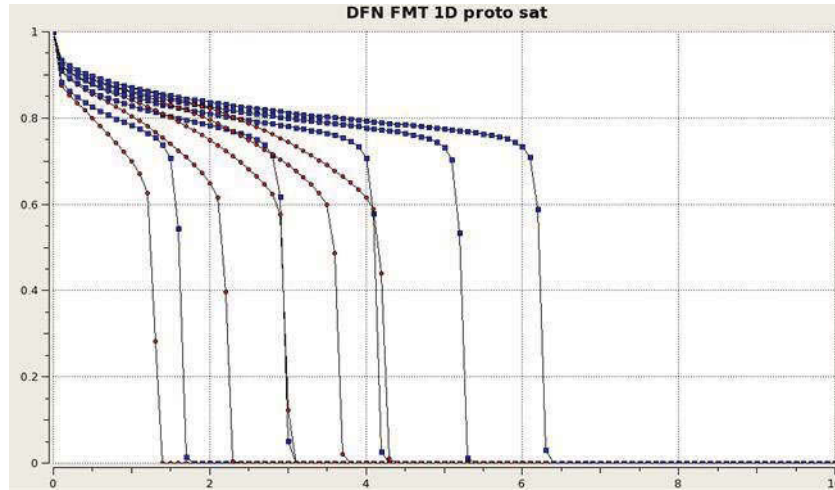


Figure 25: One dimensional waterflood from left to right (Buckley-Leverett profile). On the abscissa: distance in m. On the ordinate: Saturation with respect to water. Initially, the entire domain is fully oil saturated. An imposed pressure difference between the left and right boundary, along with a constant water saturation of 1.0 at the left causes displacement. Blue squares indicate transport without any source terms acting, red dots represent flow accounting for fracture matrix transfer by means of a source term acting on the flooded portion of the domain. The output interval with respect to time remains constant.

Figure 25 illustrates nicely the effects of a source/sink term on saturation transport. Since water saturation is displayed, we consider a sink term, accommodating the flux of water into the matrix and a corresponding transfer of oil phase into the fracture (the 1D domain of interest). This sink term acts only on parts of the domain in which the oil saturation drops below its initial level. In the case without transfer (blue squares), the saturation at the front remains constant over time, only its position advances with the direction of flow. If fracture-matrix exchange is accommodated for by the means of a sink term, however, the saturation of the front decreases in time. Also, the advancement of the front over time is not

constant, but decreases non-linearly. To summarize the most significant impact of a sink term applied on the domain of interest:

- Drop in saturation over time (with respect to water)
- Frontal advancement is not constant (with respect to front velocity), but decreases in time

The latter is illustrated in Figure 25: In the beginning, the advancement of both differs less dramatically compared to later time steps (further down the domain). So whereas the front without any sink term acting upon moves at constant speed (equal intervals between fronts), the front accounting for counter-current imbibition sees a decrease in advancement over time, and lags behind further and further.

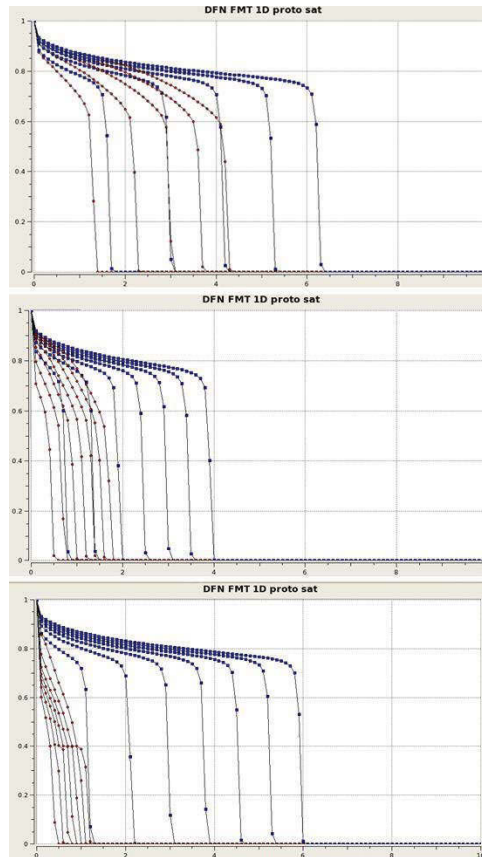


Figure 26: 1D simulations for various front speeds. From top to bottom: $1.0E-8$, $1.0E-9$ and $1.0E-11$ ms^{-1} respectively. The difference between transport without any sink term (blue curve) and accounting for sink terms gets larger increasingly.

Figure 26 illustrates that, with decreasing front velocity, saturation transport accounting for sink terms begins to stall. Whereas for a total velocity of $1.0E-8$ ms^{-1} the front with fracture-matrix transfer still makes it to about 60% of the advancement of the no fracture-matrix transfer front, this decreases dramatically to a mere 12% for the case of $1.0E-11$ ms^{-1} . This behavior causes flow to stall in small and poorly interconnected fractures with slow flow speeds. Counter-current imbibition, in these cases, ceases flow and decreases the fracture area contacted by the injected fluid. Figure 26 points out the strong rate dependence of this phenomenon. This already points to a wetted fracture surface area that depends on injection rates.

Figure 27 shows the applied sink term acting on the saturation front. Points where the front just got to are subject to the highest transfer rate, which declines exponentially towards regions which have been swept for a while already. No transfer is applied in regions which are still fully oil saturated, of course.

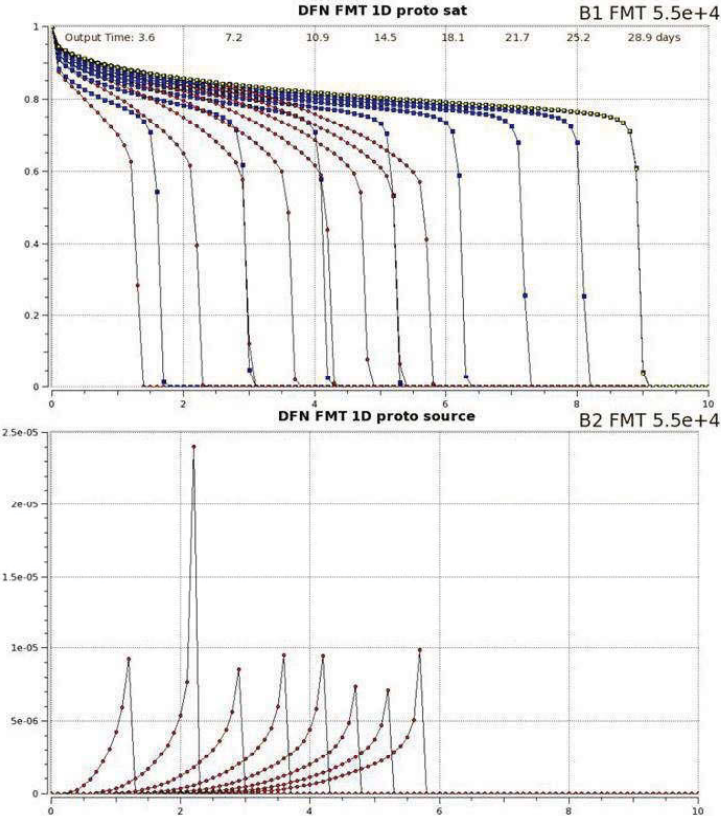


Figure 27: Top: Front advancement with (red) and without (blue) counter-current imbibition. Bottom: The magnitude of the sink term with respect to water for the corresponding front position. Note the exponential decline of the sink term away from the newly swept region (towards the left).

3.2 Results in 2D – Flow in a Single Fracture

In order to observe flow behavior in a single fracture, a two dimensional model was set up. It measures 10 m in length (x direction) and 6 m in width (y direction). It is discretized into 3410 triangular elements with 1759 nodes. An imposed waterflood from left to right was imposed by applying a constant rate boundary condition at the

left side and a constant pressure boundary at the right. Simulations were run with high and low injection rates, and hence front speed, as well as high and low matrix permeabilities, and hence high and low fracture matrix-transfer, respectively. Simulation settings common to all runs are presented in Table 2.

fracture aperture	[m]	5.0E-4
porosity	[-]	5.0E-4
permeability	[m ²]	1.04E-11
dirichlet fluid pressure @ outflow boundary	[Pa]	0.0

Table 2: Common settings for all 2D fracture simulations.

If not specified otherwise in Table 2, settings from Table 1 apply. Constant injection rates chosen were 0.5 and 0.05 m³/day as high and low scenario, respectively. An arbitrary fracture aperture of 0.5 mm was imposed, and the resulting permeability (parallel plate law, Equation 9) and porosity (see Property Scaling For Lower Dimensional Fracture Representations) was derived.

3.2.1 Low Injection Rate, High Matrix Permeability

Based on the results in 1D, it is fair to assume that a low injection rate paired with a high transfer rate results in the highest discrepancy between fracture flow with and without counter-current imbibition. This was confirmed by the simulation results of 2D scenario number one. Figure 28 illustrates:

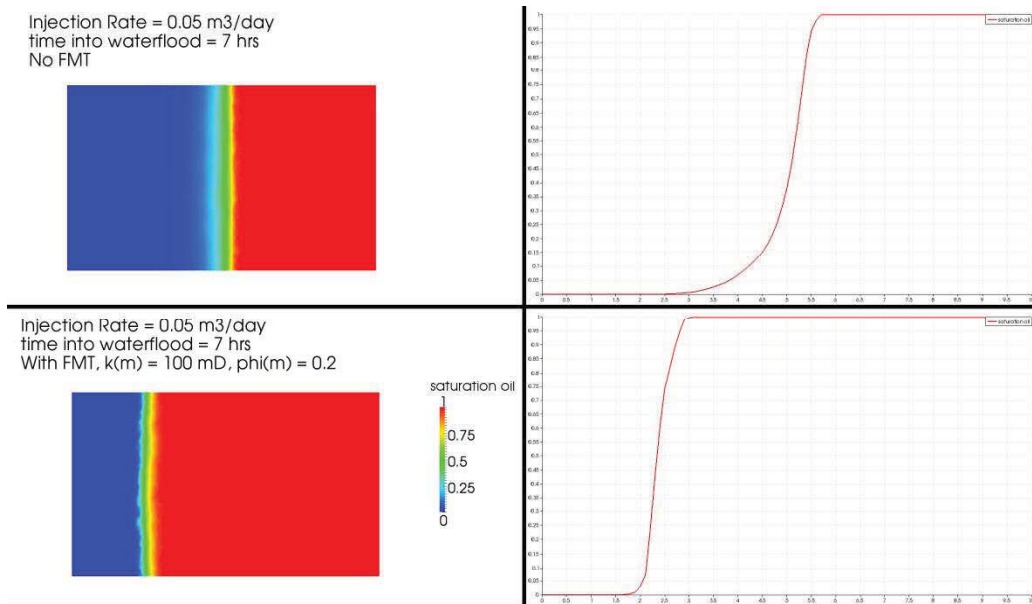


Figure 28: 2D Low rate, high matrix permeability scenario. On the left: 2D visualization of oil saturation. On the right: Oil saturation in 1D along the x-axis of the corresponding 2D plot on the left – After 7 hours of displacement from right to left. The flood front in the fracture with fracture-matrix transfer (bottom) already lags behind by about 50%.

Breakthrough occurred after about 14 hours without imbibition and after about 30 hours when imbibition was accounted for. Again, this difference is non-linear, i.e. increasing with time. The transfer of phases between fracture and virtual matrix is the largest at elements that just have been swept. Transfer behind the front ceases, as described in Results in 1D. Figure 29 illustrates the magnitude of phase exchange as the front sweeps through the fracture:

Injection Rate = 0.05 m³/day
 time into waterflood = 14 hrs
 With FMT, $k(m) = 100 \text{ mD}$, $\phi(m) = 0.2$

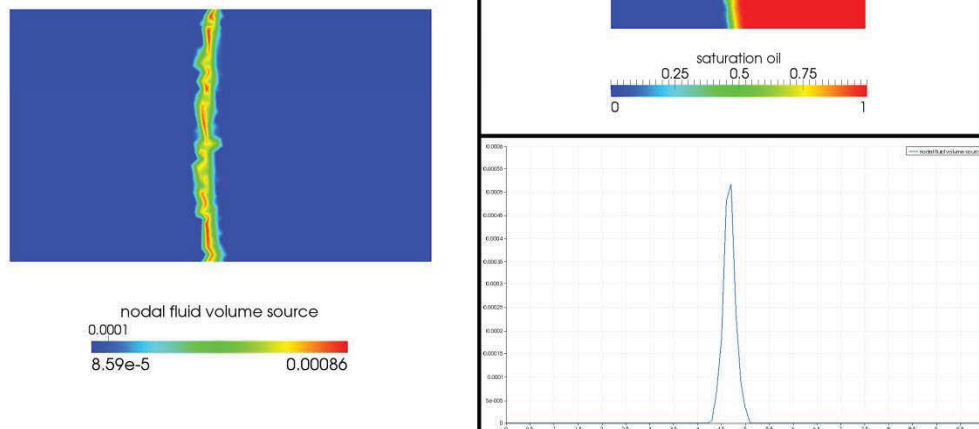


Figure 29: Illustration of transfer magnitude between the water in the fractures and the oil residing in the virtual matrix. In the transport algorithm implemented in CSMP++ by Matthäi, Geiger et al., this source term is referred to as nodal fluid volume source, as it is discretized at the nodes. Bottom right shows a 1D plot of nodal fluid volume source along the fracture's x-axis. The front is at its halfway point.

Breakthrough time of 14 hours for the no-imbibition scenario corresponds with the time it takes to fill a volume of 10 m x 6 m x 5.0E-4 (length in x-direction, length in y-direction and porosity/aperture) at the given injection rate (0.05 m³/day).

3.2.2 Low Injection Rate, Low Matrix Permeability

With a decreasing permeability assigned to the virtual matrix, the transfer is supposed to decrease in magnitude (Figure 21), hence not slowing down the advancement of the flooding front just as severely as in the high permeability scenario. Saturation at halfway is illustrated in Figure 30. Breakthrough occurred at 26 hours as compared to 30 hours with higher matrix permeability.

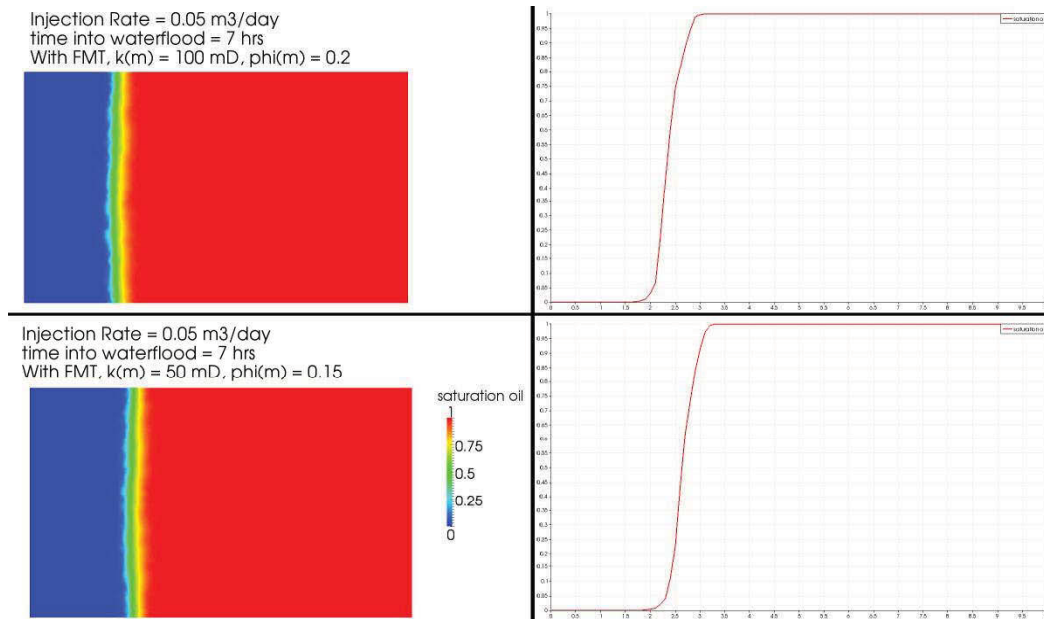


Figure 30: Comparison plot of the saturation distribution in fractures with different matrix permeabilities. Top: High conductivity matrix after 7 hours of water flooding from left to right. Bottom: Low conductivity matrix at the same time. The front is further advanced due to less phase exchange.

The cumulative volume of oil recovered from the matrix by means of counter-current transfer is 0.03448 and 0.02817 m³ for the high and low matrix permeability fracture, respectively.

3.2.3 High Injection Rate, High Matrix Permeability

For the high injection rate scenario, the fluid volume entering through the left boundary was increased tenfold, or by one order of magnitude. This results in an equivalent impact on the front speed in case of no fracture-matrix transfer. FIG shows the effects on transport due to imbibition into the virtual matrix.

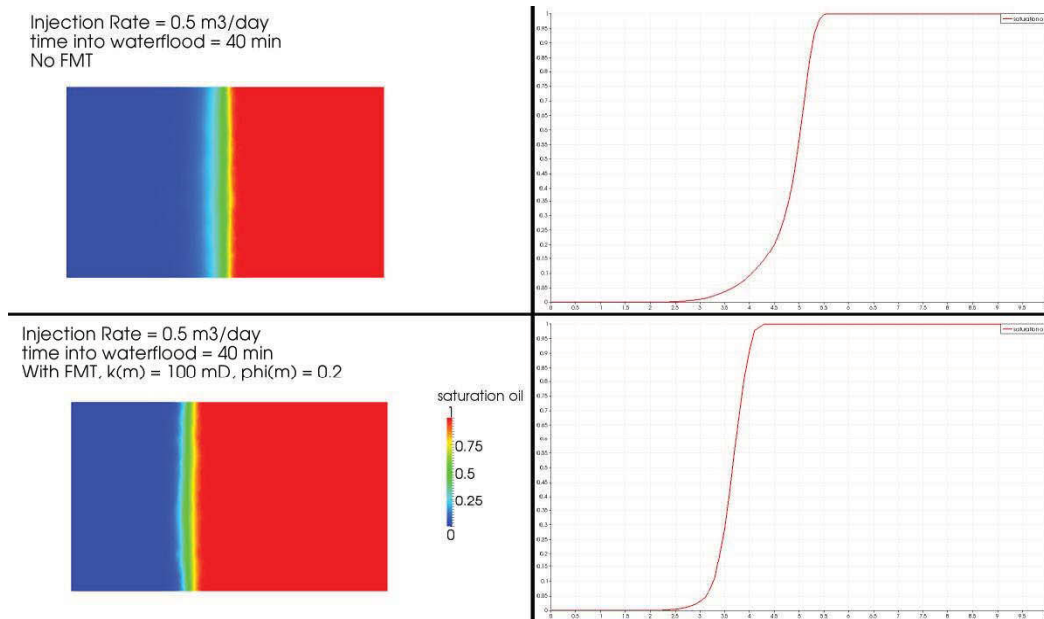


Figure 31: Advection in a single fracture for high injection rates. Top: no fracture-matrix transfer. Bottom: Transfer with a virtual matrix of relatively high conductivity.

The difference in front advancement between the no FMT and FMT simulations is far less severe for high injection rates (Figure 31) than for low injection rates (Figure 28). This is also obvious when comparing breakthrough times for the different scenarios (Table 3).

Breakthrough [hrs]	No FMT	High k(m)	Low k(m)	Δ [%]
High IR	1.36	1.8	1.7	5.5
Low IR	14	30	26	13.3

Table 3: Breakthrough times for different 2D simulation scenarios. The difference between high and low permeability matrix front speed is greater for low injection rates (slow front advancement).

3.2.4 High Injection Rate, Low Matrix Permeability

As in the low injection rate scenarios, low matrix permeability relates to faster front advancement due to less phase exchange. Since the magnitude of transfer is not as large, a lesser portion of the advancing oil water gets sucked into the adjacent rock

pores from the fracture. Due to both, earlier breakthrough (Table 3) and less recovered oil from the hydrocarbon bearing rock (Figure 32), recovery in such a case may be deemed unfavorable.

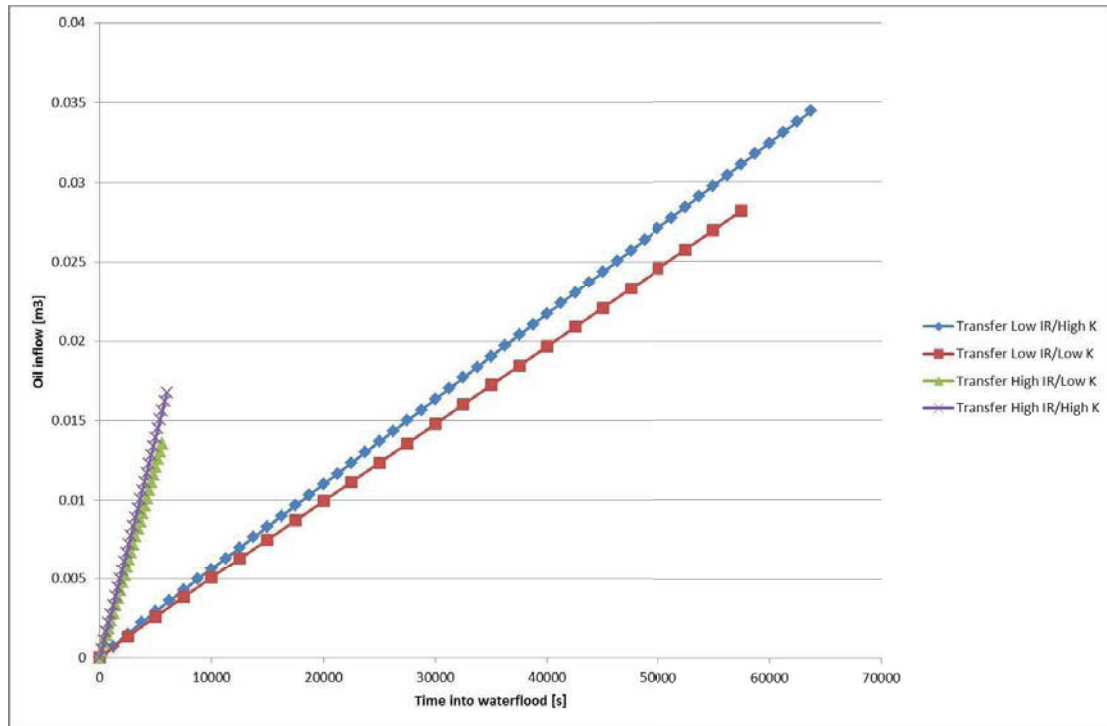


Figure 32: Oil drained into the fracture from the adjacent matrix until breakthrough for all 2D scenarios described in this section. Generally speaking, low injection rates attract more oil from the pore space. Low IR, High $k(m)$ in blue; Low IR, Low $k(m)$ in red. High IR, High $k(m)$ in purple, High IR, Low $k(m)$ in green.

3.3 Results in 3D – Discrete Fracture Network Simulations

Various simulation runs were performed, using the DFN models presented in the section on Simulation Models. A combination of different injection rates and matrix properties, similar to the approach in 2D, was used as setup in order to find the fraction of total fracture surface contacted by the injected fluid. Further, I will try to illustrate how fracture-matrix transfer effects shown in one and two dimensions in the previous section also apply in 3D.

3.3.1 Flow Channeling through NFRs due to Spatial Conductivity Variations

Figure 33 illustrates flow velocity in magnitude and direction through a couple of well interconnected fractures. Permeability distribution was generated using the mechanically controlled aperture calculation referred to earlier in this thesis. As a result of larger apertures towards the center of fractures flow tends to channel, i.e. obeys a non-uniform velocity distribution within single fractures. Also, fracture orientation relative to the global stress state effects flow focusing. An important aspect related to flow channeling, but not covered here, is the nature of fracture intersections.

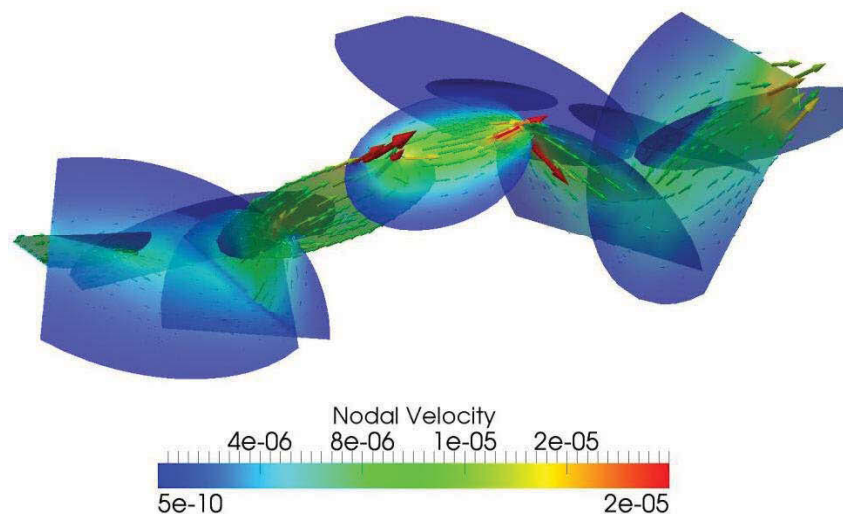


Figure 33: Flow focusing in a trivialized fracture network. Velocity distribution is far from being uniform. Flow is higher around high conductivity fractures (either due to size and/or orientation relative to stress field) and near the center of fractures.

3.3.2 JOLLY

Simulation scenarios for JOLLY once more cover combinations of high and low rate with high and low matrix permeabilities. Injection rates imposed on the constant rate inflow boundary were set to 182 and 92 m³/day of water. Matrix properties for

the high and low case were 50 and 1 mD respectively. Figure 34 shows JOLLY at breakthrough after 4.1 hours of injection for the oil wet case, i.e. without transfer/counter-current imbibition.

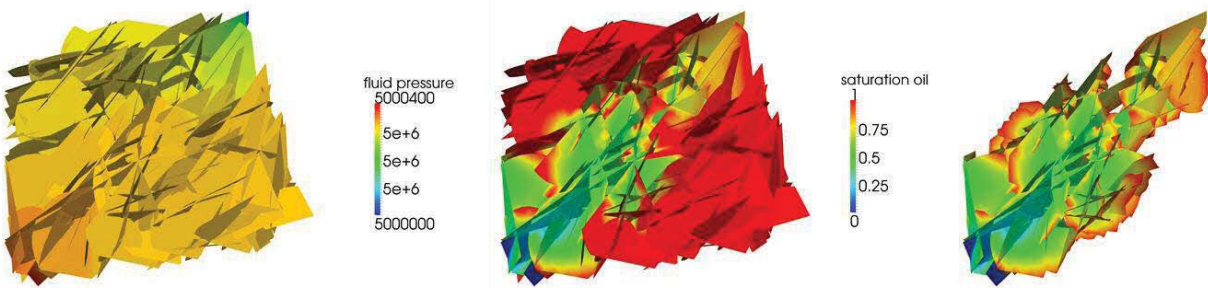


Figure 34: JOLLY after 4.1 hours of waterflooding from the bottom left to the upper right of the cube shaped domain. Left: fluid pressure distribution. Middle: saturation distribution at time of breakthrough. Right: Wetted area of the fracture network (21%).

The high rate scenario without fracture-matrix transfer results in a breakthrough time of 4.1 hours and a wetted fraction of the total surface area of 21%. We go on to compare this base case against scenarios in which imbibition into the adjacent matrix is accounted for. For the high rate high matrix permeability simulation, results are shown in Figure 35:

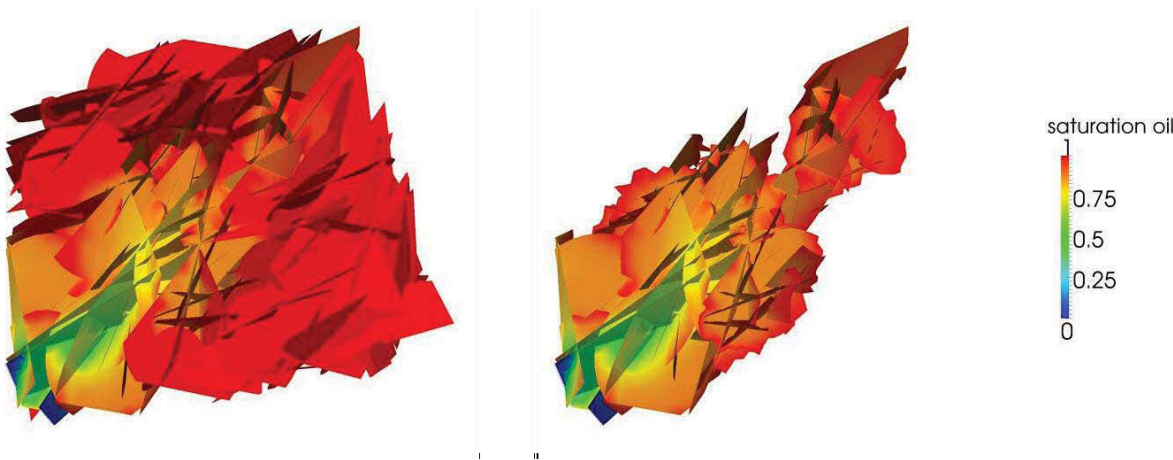


Figure 35: Saturation distribution for JOLLY at breakthrough (after 12.5 hrs) for high injection rate with high matrix permeability. On the right: wetted fraction of total contact area (14%). Note also the higher oil saturation behind the front.

Noticeable in Figure 35 are the higher oil saturation behind the flooding front, the retarded breakthrough time and the reduced fracture surface area contacted by the injected fluid. These observations coincide with the behavior of flow described bit by bit in the section on transport in one and two dimensions earlier in this chapter. For the low permeability simulation, expectations are that breakthrough is closer to the no FMT case, as well as the wetted fracture area and average saturation behind the front; obviously because the transfer will be of less magnitude as discussed previously. FIG illustrates:

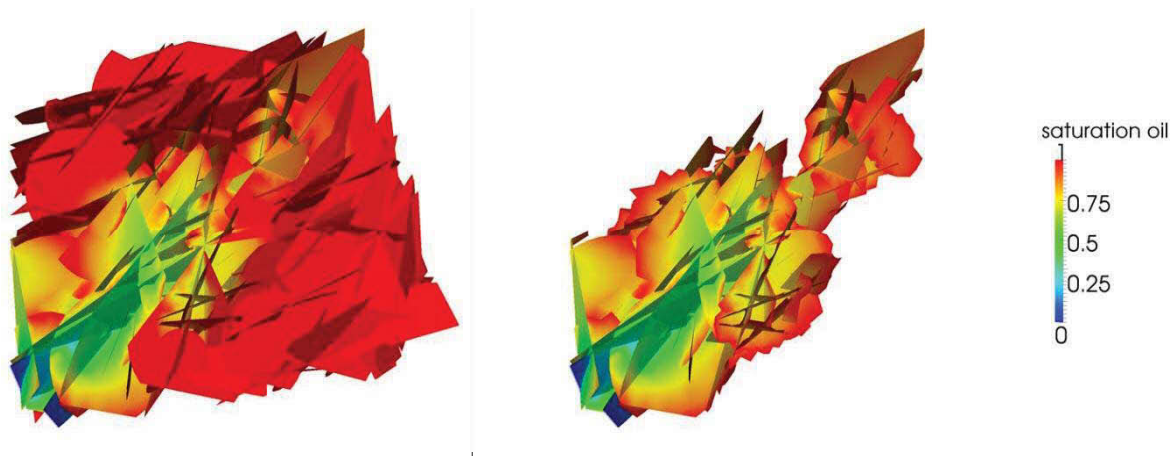


Figure 36: High injection rate (182 m³/day) and low matrix permeability (1 mD): Less transfer leads to less retardation in breakthrough (8.3 hours), a lower oil saturation behind the front and more fracture area contacted by the injected fluid (26%).

The average water saturation behind the front at time of breakthrough for the three scenarios presented thus far is 0.37, 0.18 and 0.28. Obviously, the higher the transfer, the lower the average water saturation in flooded fractures. A similar picture presents itself when comparing high and low matrix permeability scenarios for low injection rates. Table 4 summarizes the results of all JOLLY runs evaluated.

IR	k(m)	Breakthrough	Af,w	Sw,avg
high	high	12.5 hrs	14%	0.18
high	low	8.4 hrs	26%	0.28
low	high	100 hrs	20%	0.22
low	low	67 hrs	23%	0.3

Table 4: Simulation results JOLLY with FMT and various parameters

Figure 37 illustrates the wetting of fracture surface during waterflood in JOLLY. When there is little to no fracture matrix transfer, the wetted area shows little dependence on the injection rate. With higher transfer, however, the wetted area decreases in general and with increasing injection rate. For highly permeable matrix rocks, this means low injection rates lead to larger surfaces covered and made available to imbibition.

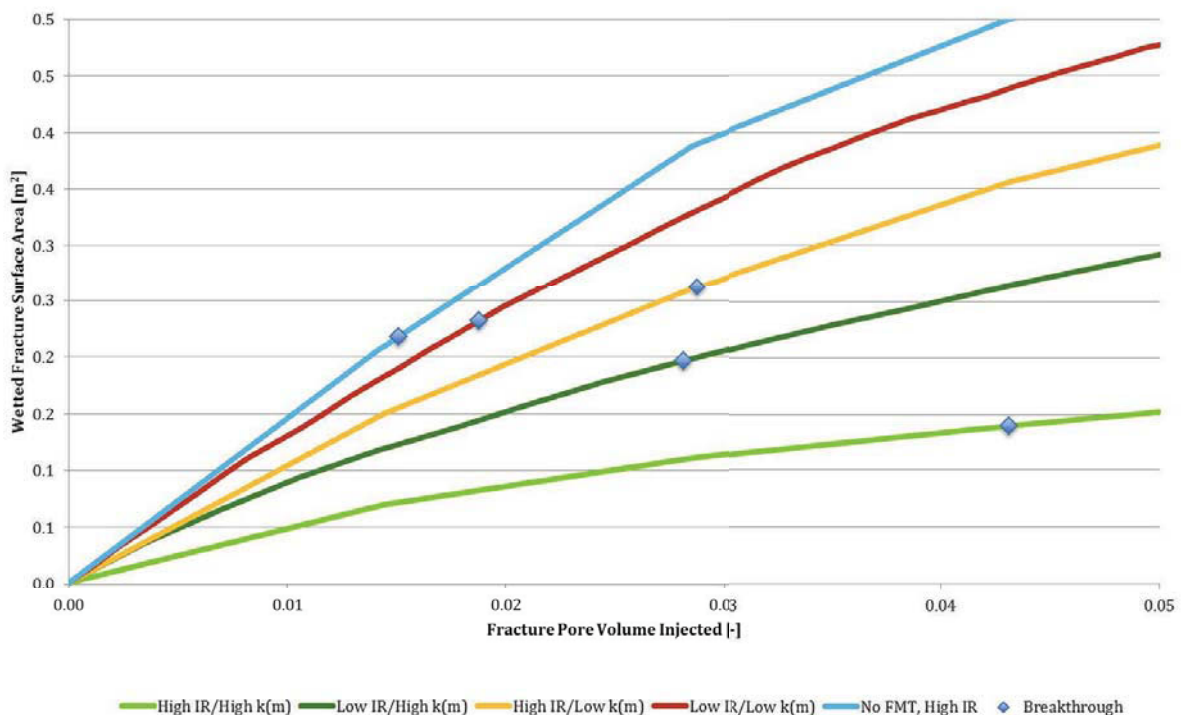


Figure 37: Plot of wetted fracture surface area vs. fracture volume injected.

3.3.3 FRACS60

The average saturation behind the flooding front is governed by the magnitude of transfer over time. Figure 38 illustrates for various injection rate to matrix permeability scenarios the difference in saturation within the fractures that provide for the main flow paths, i.e. the wetted part of the fracture network.

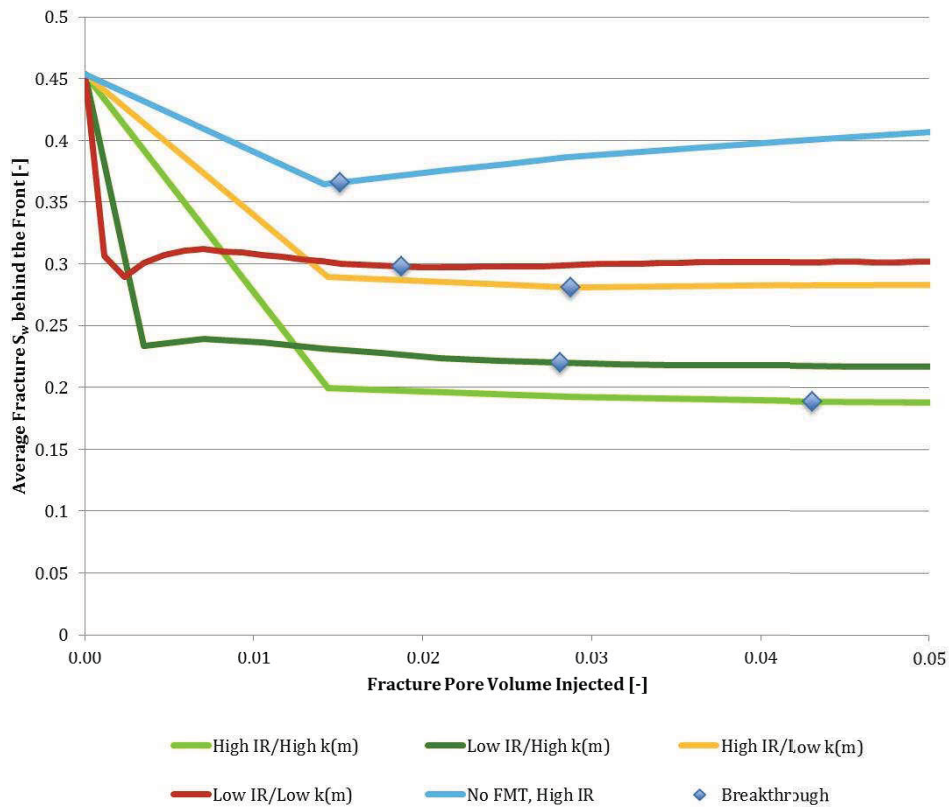


Figure 38: Average water saturation behind the front for FRACS60. Only fractures wetted by the injected fluid are considered in this average.

No significant influence of the injection rate is shown here. The dominating factor is the magnitude of capillary induced transfer. This observation has to be put

in relation with the total volume of oil drained into the fracture system and hence made available to production (Figure 39).

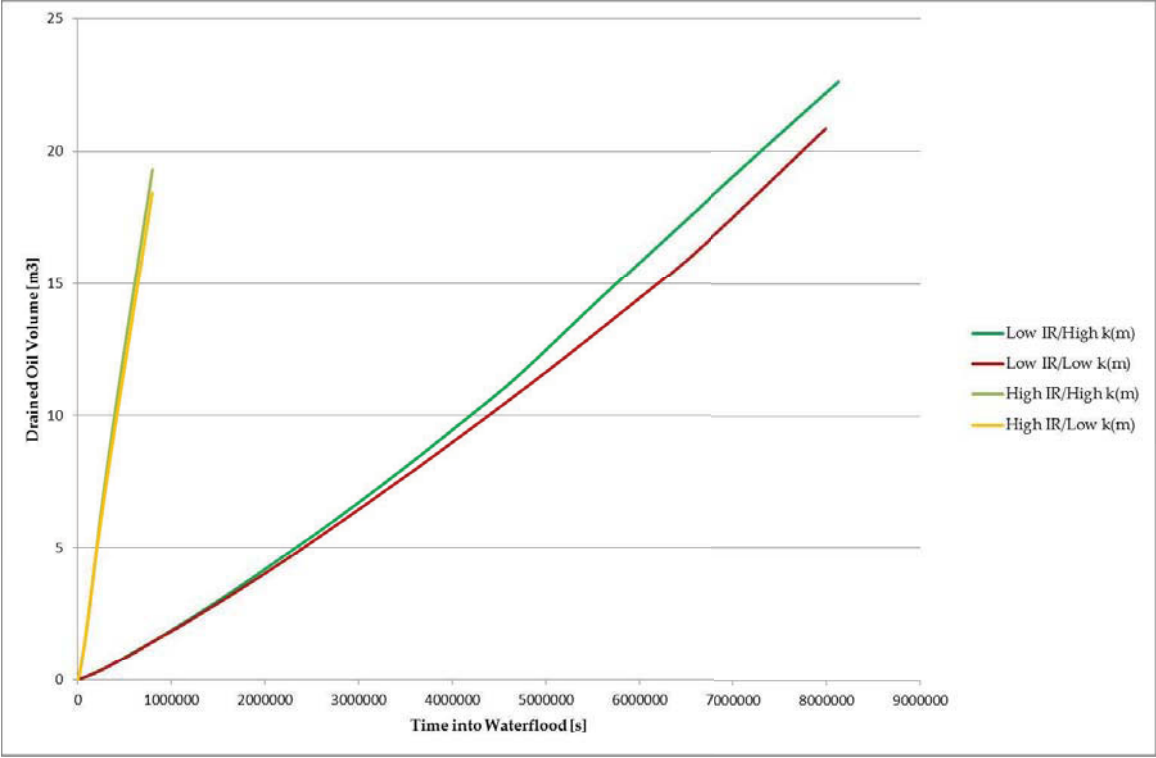


Figure 39: Drained oil volume for FRACS60 vs. time until breakthrough

Low injection rates drain more oil from the matrix until breakthrough, but it takes much longer to do so. Figure 40 shows the corresponding distribution and magnitude of transfer at time of breakthrough for FRACS60 with high and low matrix permeability.

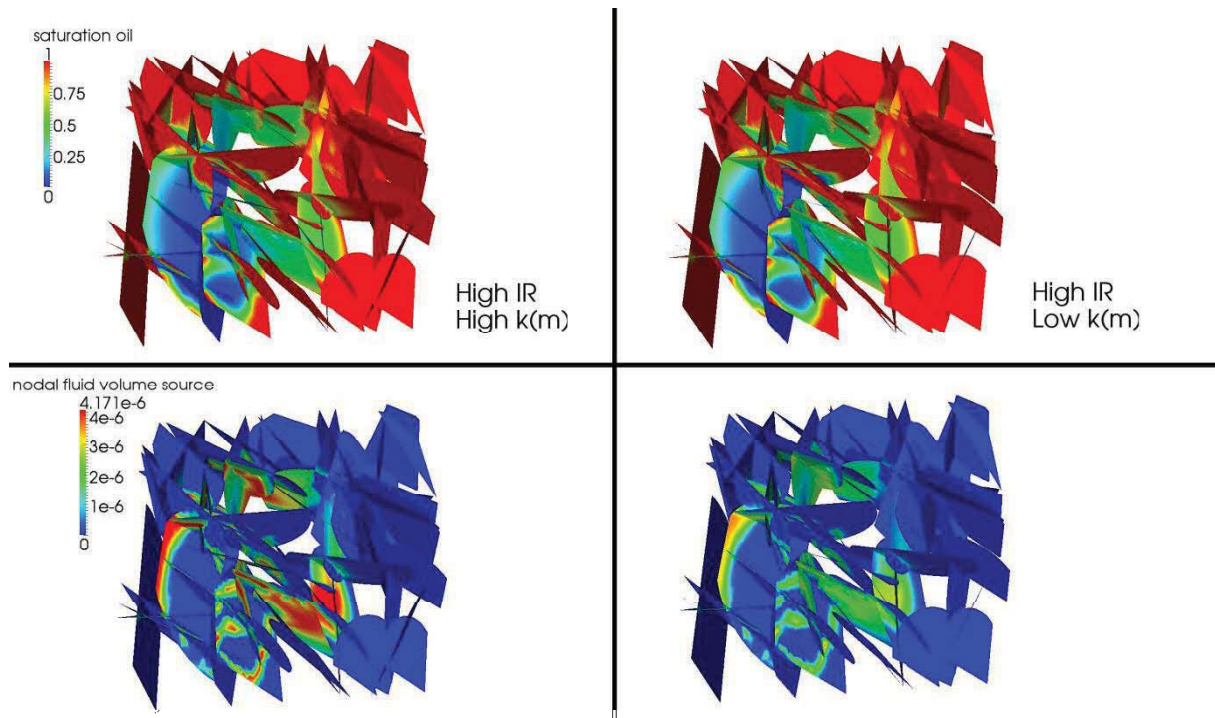


Figure 40: FRACS60 model at time of breakthrough. Left side shows saturation (top) and transfer (bottom) for the highly conductive matrix. On the right hand side: low conductivity results. Transfer in both cases is the highest in newly swept regions.

The distribution and magnitude of fracture-matrix transfer in Figure 40 reflects the findings in 1 and 2D. Areas that have been in contact with the injected water for a long period of time display almost no transfer anymore. The highly conductive matrix provides for more drainage into the fracture system as opposed to its less conductive counterpart.

4 Discussion

Transfer between fracture and adjacent matrix only occurs if contacted by the wetting fluid. Results presented in this thesis strongly indicate that this interface area is dependent on a variety of parameters, most importantly injection rate and matrix conductivity. The approach presented mimics that of a conventional dual-porosity simulation, in that no flow within the matrix domain is accounted for. As pointed out in this thesis, however, the effects of fracture-matrix transfer on flow are the most pronounced for high rock matrix permeabilities. For these types of reservoir the flow within the porous rock contributes a great deal to the overall fluid transport. Questions about the validity of the approach chosen, especially for late time-behavior, have to be raised accordingly.

Nevertheless, variations in surface area wetted still apply, and conventional dual-porosity approaches most likely fail to adapt appropriately. Flow channeling within single fractures as well as within the network as a whole govern distribution of the displacing fluid. Injection rates and transfer magnitude were shown to exert severe effects on the saturation distribution.

5 List of References

Warren, J.E. and Root, P.J.: (1963), *The Behavior of Naturally Fractured Reservoirs*. Soc. Pet. Eng. J., 245-44; *Trans., AIME*, 228.

Kazemi, H., Merrill, L., Porterfield, K. and Zeman, P. (1976), *Numerical Simulation of Water-Oil Flow in Naturally Fractured Reservoirs*. Soc. Pet. Eng. J. , 317-26; *Trans., AIME*, 261.

Nelson, R.A. (1982), *An Approach to Evaluating Fractured Reservoirs*. *Journal of Petroleum Technology*, 34(9), 2167-2170

Fourar, M. and Lenormand, R. (1998). *A Viscous Coupling Model for Relative Permeabilities in Fractures*. In *Proceedings of SPE Annual Technical Conference and Exhibition, number 1, page 6, New Orleans, Louisiana. Society of Petroleum Engineers*.

Cruikshank, K. M., Zhao, G., & Johnson, A. M. (1991). "Analysis of minor fractures associated with joints and faulted joints. *Journal of Structural Geology*, 13(8), 865–886. Elsevier.

Cruikshank, K. M., & Aydin, A. (1995). *Unweaving the joints in Entrada Sandstone, Arches National Park, Utah, USA*. *Journal of Structural Geology*, 17(3), 409–421. Elsevier.

Jolly, R., Wei, L., and Pine, R. (2000). *Stress-Sensitive Fracture-Flow Modelling in Fractured Reservoirs*. In *Proceedings of SPE International Petroleum Conference and Exhibition in Mexico, page 10, Villahermosa. Society of Petroleum Engineers*.

Matthäi, S. K., Nick, H. M., Pain, C., & Neuweiler, I. (2009). *Simulation of Solute Transport Through Fractured Rock: A Higher-Order Accurate Finite-Element Finite-Volume Method Permitting Large Time Steps*. *Transport in Porous Media*.

Paluszny, A., Matthäi, S. K., & Hohmeyer, M. (2007). *Hybrid finite element-finite volume discretization of complex geologic structures and a new simulation workflow demonstrated on fractured rocks*. *Geofluids*, 7(2), 186-208.

Unsal, E., Matthäi, S. K., & Blunt, M. J. (2009). *Simulation of multiphase flow in fractured reservoirs using a fracture-only model with transfer functions*. *Computers & Geosciences*.

Matthäi, S. K., Geiger, S., Roberts, S. G., Paluszny, A., Belayneh, M., Burri, A., et al. (2007). *Numerical simulation of multi-phase fluid flow in structurally complex reservoirs*. *Geological Society, London, Special Publications*, 292(1), 405-429.

Geiger, S., Matthäi, S. K., Roberts, S., & Zoppou, C. (2003). *Combining finite volume and finite element methods to simulate fluid flow in geologic media*. *ANZIAM Journal*, 44(April), 180-201.

Stüben, K.: *A Review of Algebraic Multigrid*, *Journal of Computational and Applied Mathematics (JCAM)* 128, pp. 281-309, 2001 (Volume 7 of JCAM Millenium Issue). Also available as GMD Report 69, November 1999.

Stüben, K.; Delaney, P.; Chmakov, S. (2003): *Algebraic Multigrid (AMG) for Ground Water Flow and Oil Reservoir Simulation*. [REDACTED]
[REDACTED]
(IGWMC), Colorado School of Mines. Golden, Colorado, Sept 17-19, 2003.

Z.N. Flynn, R.J. Pine (2007): *Fracture Characterisation Determined By Numerical Modelling Analyses*, *Proceedings of 11th ISRM Congress*, July 9 - 13, 2007 , Lisbon, Portugal

Hugo, A., Pablo, L., Tomas, Z., Monte, A., Francisco, D., James, G., et al. (2004). *Dynamic Behavior of Discrete Fracture Network (DFN) Models*. *Proceedings of SPE International Petroleum Conference in Mexico*, 1-8. Society of Petroleum Engineers.

Rogers, S., Elmo, D., Dunphy, R., & Bearinger, D. (2010). *Understanding Hydraulic Fracture Geometry and Interactions in the Horn River Basin Through DFN and Numerical Modeling*. *Canadian Unconventional Resources and International Petroleum Conference* (pp. 1-12).

Ishibashi, T., Watanabe, N., Hirano, N., Okamoto, A., & Tsuchiya, N. (2009). *Development of Discrete Fracture Network Model Simulator, GeoFlow, for Evaluation of Three Dimensional Channeling Flow*. *Proceedings of International Petroleum Technology Conference*. Society of Petroleum Engineers.

Chung, T. J. (2002): *Computational Fluid Dynamics*. Cambridge University Press, Cambridge.

Henderson, G. D., Danesh, A., Tehrani, D. H., & Peden, J. M. (1997). *The effect of velocity and interfacial tension on relative permeability of gas condensate fluids in the wellbore region*. *Journal of Petroleum Science and Engineering*, 17(3-4), 265-273.

Henderson, G. D., Danesh, A., Tehrani, D. H., & Al-Kharusi, B. (2000). *The Relative Significance of Positive Coupling and Inertial Effects on Gas Condensate Relative Permeabilities at High Velocity*. *SPE Annual Technical Conference and Exhibition*. Dallas, Texas: 2000,. Society of Petroleum Engineers Inc.

6 Appendix

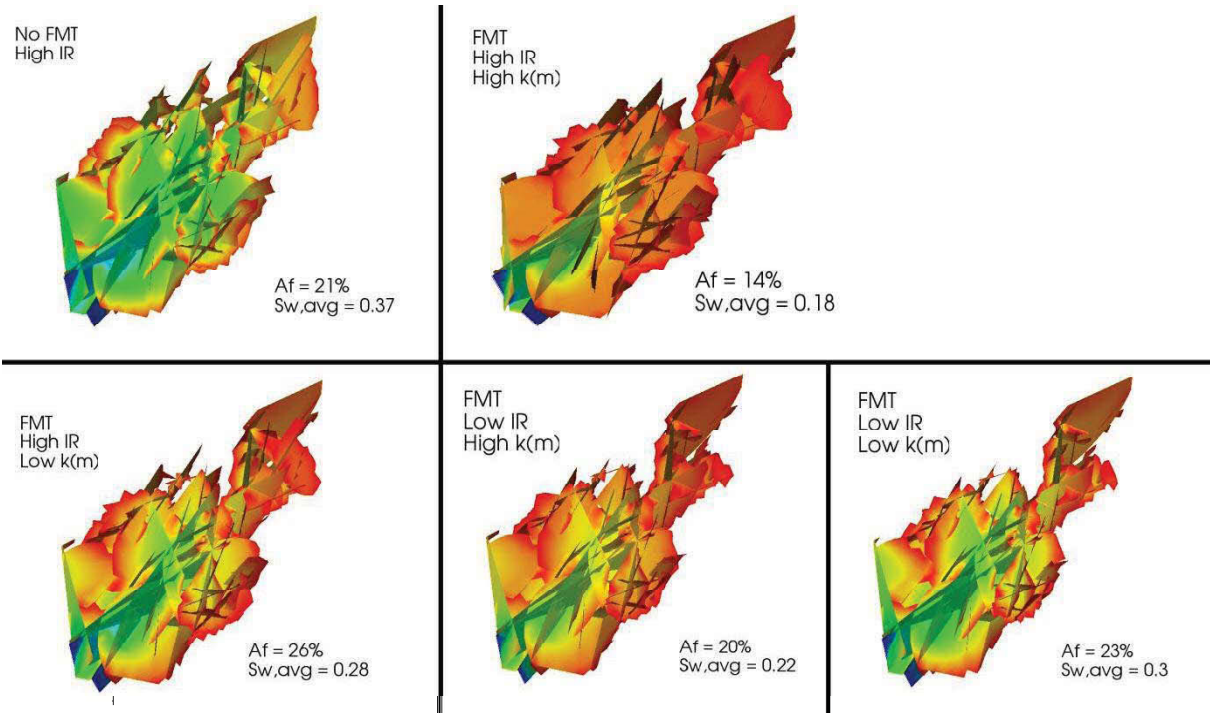


Figure 41: Comparison of fraction of surface area wetted at time of breakthrough for different setups in JOLLY.